CrossMark

JADES: Resolving the Stellar Component and Filamentary Overdense Environment of Hubble Space Telescope (HST)-dark Submillimeter Galaxy HDF850.1 at $z = 5.18$

Fengwu Sun[1] , Jakob M. Helton[1] , Eiichi Egami[1] , Kevin N. Hainline[1] , George H. Rieke[1] , Christopher N. A. Willmer[1] ,
Daniel J. Eisenstein[2] , Benjamin D. Johnson[2] , Marcia J. Rieke[1] , Brant Robertson[3] , Sandro Tacchella[4,5] ,
Stacey Alberts[1] , William M. Baker[4,5] , Rachana Bhatawdekar[6,7] , Kristan Boyett[8,9] , Andrew J. Bunker[10] ,
Stephane Charlot[11] , Zuyi Chen[1] , Jacopo Chevallard[10] , Emma Curtis-Lake[12] , A. Lola Danhaive[4,5] ,
Christa DeCoursey[1] , Zhiyuan Ji[1] , Jianwei Lyu[1] , Roberto Maiolino[4,13,14] , Wiphu Rujopakarn[15,16] , Lester Sandles[4,5] ,
Irene Shivaei[1] , Hannah Übler[4,5] , Chris Willott[17] , and Joris Witstok[4,5]

[1] Steward Observatory, University of Arizona, 933 N. Cherry Avenue, Tucson, AZ 85721, USA; fengwusun@arizona.edu
[2] Center for Astrophysics, Harvard & Smithsonian, 60 Garden Street, Cambridge, MA 02138, USA
[3] Department of Astronomy and Astrophysics, University of California, Santa Cruz, 1156 High Street, Santa Cruz, CA 95064, USA
[4] Kavli Institute for Cosmology, University of Cambridge, Madingley Road, Cambridge, CB3 0HA, UK
[5] Cavendish Laboratory, University of Cambridge, 19 JJ Thomson Avenue, Cambridge, CB3 0HE, UK
[6] European Space Agency (ESA), European Space Astronomy Centre (ESAC), Camino Bajo del Castillo s/n, E-28692 Villanueva de la Cañada, Madrid, Spain
[7] European Space Agency, ESA/ESTEC, Keplerlaan 1, 2201 AZ Noordwijk, The Netherlands
[8] School of Physics, University of Melbourne, Parkville 3010, VIC, Australia
[9] ARC Centre of Excellence for All Sky Astrophysics in 3 Dimensions (ASTRO 3D), Australia
[10] Department of Physics, University of Oxford, Denys Wilkinson Building, Keble Road, Oxford OX1 3RH, UK
[11] Sorbonne Université, CNRS, UMR 7095, Institut d'Astrophysique de Paris, 98 bis bd Arago, F-75014 Paris, France
[12] Centre for Astrophysics Research, Department of Physics, Astronomy and Mathematics, University of Hertfordshire, Hatfield AL10 9AB, UK
[13] Cavendish Laboratory—Astrophysics Group, University of Cambridge, 19 JJ Thomson Avenue, Cambridge, CB3 0HE, UK
[14] Department of Physics and Astronomy, University College London, Gower Street, London WC1E 6BT, UK
[15] National Astronomical Research Institute of Thailand, Don Kaeo, Mae Rim, Chiang Mai 50180, Thailand
[16] Department of Physics, Faculty of Science, Chulalongkorn University, 254 Phayathai Road, Pathumwan, Bangkok 10330, Thailand
[17] NRC Herzberg, 5071 West Saanich Road, Victoria, BC V9E 2E7, Canada

Abstract

HDF850.1 is the brightest submillimeter galaxy (SMG) in the Hubble Deep Field. It is known as a heavily dust-obscured star-forming galaxy embedded in an overdense environment at $z = 5.18$. With nine-band NIRCam images at 0.8–5.0 μm obtained through the JWST Advanced Deep Extragalactic Survey, we detect and resolve the rest-frame UV–optical counterpart of HDF850.1, which splits into two components because of heavy dust obscuration in the center. The southern component leaks UV and Hα photons, bringing the galaxy $\sim$100 times above the empirical relation between infrared excess and UV continuum slope (IRX–β_{UV}). The northern component is higher in dust attenuation and thus fainter in UV and Hα surface brightness. We construct a spatially resolved dust-attenuation map from the NIRCam images, well matched with the dust continuum emission obtained through millimeter interferometry. The whole system hosts a stellar mass of $10^{10.8\pm0.1}$ $M_\odot$ and star formation rate (SFR) of $10^{2.8\pm0.2}$ $M_\odot$ yr^{-1}, placing the galaxy at the massive end of the star-forming main sequence at this epoch. We further confirm that HDF850.1 resides in a complex overdense environment at $z = 5.17$–5.30, which hosts another luminous SMG at $z = 5.30$ (GN10). The filamentary structures of the overdensity are characterized by 109 Hα-emitting galaxies confirmed through NIRCam slitless spectroscopy at 3.9–5 μm, of which only eight were known before the JWST observations. Given the existence of a similar galaxy overdensity in the GOODS-S field, our results suggest that 50% $\pm$ 20% of the cosmic star formation at $z = 5.1$–5.5 occur in protocluster environments.

Unified Astronomy Thesaurus concepts: High-redshift galaxies (734); Luminous infrared galaxies (946); Ultraluminous infrared galaxies (1735); Galaxy evolution (594); James Webb Space Telescope (2291)

Supporting material: figure set, machine-readable table

1. Introduction

In the local Universe, the population of ultra-luminous infrared galaxies (ULIRGs, with IR luminosities $L_{IR} > 10^{12}$ $L_\odot$) hosts vigorous dust-obscured star formation. In the distant Universe at redshift $z \gtrsim 1$, galaxies with similar luminosities have been routinely discovered with submillimeter and/or millimeter and infrared sky surveys. The Spitzer Space Telescope provided detailed information out to redshifts of $z \simeq 2$–3 (e.g., Armus et al. 2020), but at higher redshifts, the infrared excess emission moves into the far-infrared, and the negative K-correction strongly favors discoveries at submillimeter and millimeter wavelengths. Some of these galaxies, with flux densities of $\gtrsim 1$ mJy at submillimeter wavelengths, are classified as submillimeter galaxies (SMGs; see a recent review by Hodge & da Cunha 2020).

Since the first discoveries around the end of the last century (e.g., Smail et al. 1997; Hughes et al. 1998; Ivison et al. 1998), the identification of the rest-frame optical (i.e., stellar) counterparts has remained ambiguous for certain high-redshift SMGs

with strong dust obscuration. This was partially caused by the coarse angular resolution of single-dish submillimeter telescopes, for example, $\theta \sim 15''$ with the 15 m James Clerk Maxwell Telescope at 850 μm. However, even with (sub) arcsec resolution dust continuum images obtained with millimeter interferometers including the Atacama Large Millimeter Array (ALMA), Submillimeter Array (SMA), Plateau de Bure Interferometer (PdBI) and its successor Northern Extended Millimeter Array, it is still challenging to detect the counterparts of certain SMGs in optical and near-IR wavelengths.

Recent ALMA continuum observations have suggested that 15%–20% of SMGs remain undetected in deep ground-based K-band images ($K > 24.4$, Simpson et al. 2014; $K > 25.3$, Dudzevičiūtė et al. 2020; Smail et al. 2021; AB magnitude system is used throughout this paper). Similar percentages of optical and/or near-IR-dark SMGs are also seen with the SMG samples observed with Hubble Space Telescope (HST)/WFC3-IR ($H_{160} \gtrsim 27$, e.g., Chen et al. 2015; Franco et al. 2018; Yamaguchi et al. 2019; Casey et al. 2021; Gómez-Guijarro et al. 2022a; Sun et al. 2022a; Fujimoto et al. 2023), and these galaxies are often referred to as HST-dark, H-dropout (not to confuse with Lyman-break galaxies at $z \gtrsim 12$), or H-faint galaxies. These galaxies are thought to be objects with high dust attenuation ($A_V \gtrsim 3$) and at high redshifts ($z \simeq 3$–6), which could contribute to $\sim 10\%$ of the cosmic SFR density at this epoch (e.g., Alcalde Pampliega et al. 2019; Wang et al. 2019; Williams et al. 2019; Yamaguchi et al. 2019; Dudzevičiūtė et al. 2020; Sun et al. 2021a).

As the brightest SMG discovered in the Hubble Deep Field-North (HDF; Hughes et al. 1998), HDF850.1 is known as one of the earliest examples of optical and/or near-IR-dark SMGs. Early tentative optical and/or near-IR counterpart identifications (Hughes et al. 1998; Downes et al. 1999; Dunlop et al. 2004) have been ruled out with increasing accuracy of dust continuum position through high-resolution SMA (Cowie et al. 2009) and PdBI (Walter et al. 2012; Neri et al. 2014) observations. The source remains undetected even with the deep HST/WFC3-IR imaging obtained through the CANDELS survey ($J_{125} > 28.2$, $H_{160} > 27.3$; Grogin et al. 2011; Koekemoer et al. 2011; Serjeant & Marchetti 2014). With the detections of multiple CO and [C II] transitions using the PdBI, Walter et al. (2012) spectroscopically confirmed that HDF850.1 is an SMG at $z = 5.183$ (also Neri et al. 2014; Riechers et al. 2020), which resides in a galaxy overdensity at $z \sim 5.2$ in the GOODS-N field (see also Arrabal Haro et al. 2018; Calvi et al. 2021, 2023).

The great imaging sensitivity and angular resolution of the JWST/NIRCam (Rieke et al. 2023b) have offered us an unprecedented opportunity to resolve the rest-frame optical morphology of HST-dark dusty star-forming galaxies at $z \simeq 3$–6 (e.g., Barrufet et al. 2023; Cheng et al. 2023; Kokorev et al. 2023; McKinney et al. 2023; Nelson et al. 2023; Pérez-González et al. 2023; Rodighiero et al. 2023; Smail et al. 2023), which was previously impossible with HST, Spitzer/IRAC, or any ground-based facilities unless with the aid of gravitational lensing (see Sun et al. 2021a).

In this paper, we present nine-band NIRCam imaging observation of HDF850.1 obtained through the JWST Advanced Deep Extragalactic Survey (JADES), a guaranteed-time observation program aiming to study the formation and evolution of galaxies from $z \sim 15$ to the present Universe. We detect and resolve the stellar component of HDF850.1, solving the puzzle of its optical counterpart identification, which has been unclear since

its discovery (Hughes et al. 1998). Moreover, combining with public NIRCam wide-field slitless spectroscopy (WFSS) observations at 3.9–5.0 μm (Oesch et al. 2023), we also confirm 109 galaxies at $z = 5.17$–5.30 through the detections of Hα emission, including the eight galaxies previously confirmed through ground-based spectroscopy. Our study unveils four galaxy groups across a comoving line-of-sight (LOS) distance of ~ 60 Mpc, whose 3D distribution resembles filaments of cosmic webs seen with simulations (e.g., Bond et al. 1996). Through this work, we demonstrate the capability of JWST/NIRCam in resolving the dust-obscured stellar component and large-scale structures of high-redshift galaxies through imaging and spectroscopy.

This paper is arranged as follows: In Section 2, we describe the observations and corresponding data reduction techniques. Section 3 presents the photometric and spectroscopic measurements of HDF850.1 and Hα-emitting galaxies in the GOODS-N field at $z_{\rm spec} = 5.1$–5.5. We study the physical properties and overdense environment of HDF850.1 in Section 4. The summary is in Section 6. Throughout this work, we assume a flat ΛCDM cosmology with $H_0 = 70$ km s^{-1} Mpc^{-1}, and $\Omega_{\rm M} = 0.3$. We also assume a Chabrier (2003) initial mass function (IMF). We define the IR luminosity ($L_{\rm IR}$) as the integrated luminosity over a rest-frame wavelength range from 8 to 1000 μm.

2. Observation and Data Reduction

2.1. Imaging

We conducted JWST/NIRCam imaging observations in the GOODS-N field through the JADES program (project ID, hereafter PID: 1181; PI: Eisenstein) in early 2023 February. The detailed observation design is presented in Eisenstein et al. (2023). Our NIRCam observations consist of three medium-depth pointings with MIRI as parallel instrument (12.2 hr in total; the NIRCam data were partially presented in Tacchella et al. 2023), and four deeper pointings with NIRSpec as primary instrument (31.5 hr in total; the NIRSpec data were partially presented in Bunker et al. 2023). The total NIRCam survey area is ~ 56 arcmin^2 in the GOODS-N field by 2023 February 8. We used nine photometric filters from 0.8 to 5.0 μm, including F090W, F115W, F150W, F200W, F277W, F335M, F356W, F410M, and F444W filters. The total exposure time at the location of HDF850.1 (R.A.: 12:36:51.980, decl.: $+62°12'25''.7$) is 6.30 hr in the F115W band and 3.15 hr in each of the other eight bands.

The NIRCam imaging data reduction techniques will be presented in a forthcoming paper from the JADES Collaboration (S. Tacchella et al. 2023, in preparation), and we also refer the readers to Tacchella et al. (2023), Rieke et al. (2023a). The data were initially processed with the standard JWST calibration pipeline v1.9.2. The JWST Calibration Reference Data System context map "jwst_1039.pmap" is used, including the flux calibration for JWST/NIRCam from Cycle 1. Customized steps were included for the removal of the so-called "1/f" noise, "wisp," and "snowball" artifacts (see Rigby et al. 2023). Because the current long-wavelength (LW; 2.5–5.0 μm) flat-field data in the pipeline could introduce small artifacts in the background, we also used customized sky-flats for the LW filters, which were constructed using the deep imaging data obtained with JADES and other public programs (see Tacchella et al. 2023). The world coordinate system (WCS) positions of all individual images were registered to a reference catalog, which was constructed from the HST

Previous HST and Spitzer/IRAC Images:
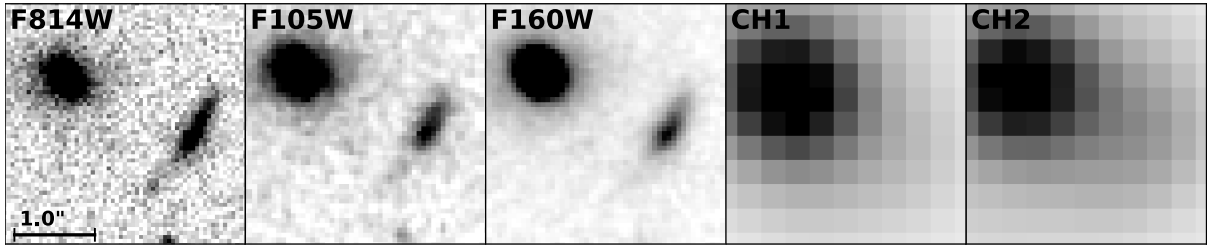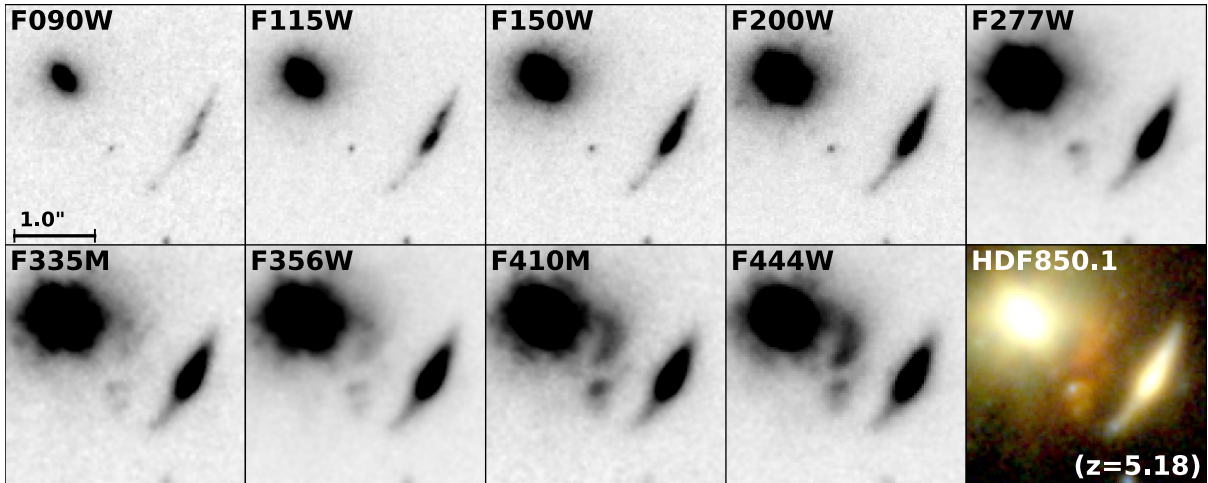
JADES JWST/NIRCam Images:

Figure 1. Top: HST F814W/F105W/F160W and Spitzer/IRAC Channel 1/2 (3.6/4.5 μm) images at the location of HDF850.1. Image sizes are $3'' \times 3''$ (north up, east left). HDF850.1 is not detected in HST images and blended with two foreground galaxies in IRAC images. Bottom: same but for JWST/NIRCam cutout images. The last panel shows a false-color image produced using all NIRCam data. The southern component of HDF850.1 is detected in all nine NIRCam bands, and the northern component is only detected with the LW filters (F277W – F444W).

mosaics in the GOODS-N field with astrometry tied to the Gaia-EDR3 catalog (Gaia Collaboration et al. 2021; G. Brammer 2023, private communication). Finally, the calibrated images are mosaicked to a common WCS with a pixel size of $0\rlap{.}''03$ and drizzle parameter of `pixfrac = 1`.

When applicable, we also used the HST/Advanced Camera for Surveys (ACS) mosaics in the F435W, F606W, F775W, F814W, and F850LP bands that were produced as part of the Hubble Legacy Fields project (HLF v2.5; Whitaker et al. 2019). Spitzer/IRAC mosaics in Channel 1/2 produced by the GOODS Re-ionization Era wide-Area Treasury from Spitzer project (Stefanon et al. 2021) are also used, but only for display purpose.

2.2. Grism Spectroscopy

The JWST/NIRCam WFSS observations of the GOODS-N field were obtained on UT 2023 February 11–13 through the First Reionization Epoch Spectroscopic COmplete Survey (FRESCO; Oesch et al. 2023; PI: Oesch, PID: 1895). FRESCO observed both the GOODS-N and GOODS-S fields using the row-direction grisms on both modules of NIRCam with the F444W filter (3.9–5.0 μm). The spectral resolution is $R \sim 1600$ at 4 μm. The total overlapping area between the JADES and FRESCO footprints is ~ 35 arcmin^2 in GOODS-N. The total spectroscopic observing time for FRESCO per GOODS field is ~ 16 hr with a typical on-source time of ~ 2 hr.

A detailed description of the JWST/NIRCam grism data reduction can be found in Sun et al. (2023), Helton et al. (2023). Starting from the stage-1 products of the JWST

standard pipeline, we assigned WCS information, performed flat-fielding, and subtracted out the σ-clipped median sky background from each individual exposure. Because we are interested in conducting a targeted emission-line search, and we do not expect any of our $z > 5$ Hα-emitting galaxies to have a strong continuum that is detectable with grism spectroscopy, we utilized a median-filtering technique to subtract out any remaining continuum or background on a row-by-row basis following the methodology of Kashino et al. (2023). This produces emission-line maps for each grism exposure without continuum emission. Short-wavelength (SW) NIRCam observations were used for the astrometric calibration of the LW WFSS data taken simultaneously. Under the assumption that the internal alignment between NIRCam SW and LW detectors is stable, this effectively provides wavelength calibration of grism spectra (see Sun et al. 2023). We used the spectral tracing, grism dispersion, and flux calibration models that were produced using the JWST/NIRCam commissioning or Cycle-1 calibration data (PIDs: 1076, 1536, 1537, 1538; Sun et al. 2022b, 2023).[18]

3. Results

3.1. Detection and Photometry of HDF850.1

Figure 1 presents the HST, Spitzer/IRAC, and JWST/NIRCam cutout images of HDF850.1 at $z = 5.185$ (Neri et al. 2014). HDF850.1 locates between the $z = 1.224$ elliptical galaxy in the top left corner (Barger et al. 2008), and the

---

[18] https://github.com/fengwusun/nircam_grism

$z_{\mathrm{phot}} = 2.02^{+0.08}_{-0.15}$ elongated galaxy on the right. The photometric redshift of this elongated galaxy is estimated from our NIRCam data (Hainline et al. 2023), which is slightly higher than the literature value, $z_{\mathrm{phot}} \sim 1.75$ (e.g., Fernández-Soto et al. 1999; Rowan-Robinson 2003).

HDF850.1 is not detected in these HST images, and it is blended with the two foreground galaxies in the Spitzer/IRAC bands. Therefore, there was no robust detection of the stellar continuum for HDF850.1 before the launch of the JWST, although we note that Serjeant & Marchetti (2014) reported the detection of HDF850.1 in deblended IRAC Channel 3/4 (5.8 and 8 μm) images. Given the coarse resolution of IRAC (the full width of half maximum of the point-spread function, hereafter PSF, is $\sim 2''$), HDF850.1 is not resolved separately at these wavelengths.

HDF850.1 is detected and resolved in our nine-band NIRCam images. At $z = 5.185$, the 4000 Å break of HDF850.1 is redshifted to 2.5 μm, which is similar to the dichroic wavelength between the NIRCam SW and LW channel. The source is split into a northern and a southern component in the LW filters (F277W − F444W; rest-frame optical), dubbed as HDF850.1-N and HDF850.1-S, respectively. In the SW filters (F090W − F200W; rest-frame UV), the northern component is not detected, while the southern component is detected as a compact source.

To measure the flux densities of HDF850.1 in a consistent way across all NIRCam wavelengths, we first subtract the two foreground galaxies to the northeast and west of HDF850.1 through morphological modeling with GALFIT (Peng et al. 2010). The $z = 1.224$ elliptical galaxy is fitted with two Sérsic profiles to account for compact and extended light components, and the $z \sim 2$ galaxy is fitted with single Sérsic profile. Source centroids of these two galaxies are fixed in the fitting, while their effective radii (R_{e}), axis ratios (b/a), Sérsic indices, and position angles are allowed to float. We also include one or two Sérsic profiles to model the light from HDF850.1. The best-fit models of two foreground galaxies are then subtracted from our NIRCam images. The remaining residual within $0''.3$ of the northeast elliptical galaxy is about $\sim 1\%$ of its total brightness, suggesting an overall good quality of subtraction at the present PSF accuracy.

In order to study the spatially resolved color information, we homogenize the PSF of NIRCam images in the F090W–F410M filters to that of the F444W filter. As illustrated in Tacchella et al. (2023), we first derive empirical PSF (ePSF) using ~ 10 stars with the PHOTUTILS package (Bradley et al. 2022). We then construct PSF matching kernels with PHOTUTILS assuming a top-hat or cosine bell window function. The PSF encircled energy functions after kernel convolution agree with that in the F444W band within 1%, similar to the accuracy reported in Chen et al. (2023).

The neighbor-subtracted PSF-matched NIRCam images of HDF850.1 are presented in Figure 2. We construct the detection map of HDF850.1 by stacking the NIRCam images obtained above 3 μm. We then produce image segmentation with PHOTUTILS by finding sources with 40 pixels detected above 5σ in the detection map. Sources are deblended with standard parameters `nlevels=32` and `contrast=0.001`. This allows the deblending of HDF850.1 into two components (-N/S) as shown in solid red lines in Figure 2. We conduct aperture photometry using these segments. The northern segment is affected by the residual light from the $z = 1.224$ elliptical galaxy in the SW filters, resulting in artificial detections of HDF850.1-N

in these bands that are rejected by visual inspection. Therefore, in practice, we use smaller segments constructed with a higher signal-to-noise ratio (S/N) threshold at 10. An aperture correction factor of 1.29 is utilized, which is derived from the median flux ratio between 5σ and 10σ segments in the LW filters. The photometric uncertainty is derived using both the error extension of our image mosaics and the root mean square of the residual images. Similar to Tacchella et al. (2023), we adopt a 5% error floor for our photometric measurements (Table 1) to account for potential uncertainties from photometric zero-points and instrument flat fields.

3.2. Lens Model

HDF850.1 is mildly lensed by the $z = 1.224$ elliptical galaxies to the northeast (e.g., Hogg et al. 1996; Hughes et al. 1998; Downes et al. 1999; Dunlop et al. 2004; Cowie et al. 2009; Walter et al. 2012; Neri et al. 2014). With the latest JWST/NIRCam observation, we reconstruct the lens model using software LENSTOOL (Jullo et al. 2007). Similar to that in Neri et al. (2014), we model the lens as an elliptical singular isothermal sphere with a redshift of $z_l = 1.224$ (Barger et al. 2008). Instead of assuming a velocity dispersion of 150 km s^{-1} used by Dunlop et al. (2004), Neri et al. (2014), we performed JWST/NIRCam spectral energy distribution (SED) modeling of the lens with code CIGALE (Boquien et al. 2019), and we derived a stellar mass of $M_{\mathrm{star}} = 10^{10.8 \pm 0.1}\ M_{\odot}$. With an effective radius of $R_{\mathrm{e}} = 1.7 \pm 0.2$ kpc measured by NIRCam, we estimate a velocity dispersion of $\sigma = \sqrt{GM_{\mathrm{star}}/5R_{\mathrm{e}}} \sim 180$ km s^{-1}. The coordinate and ellipticity (0.40) are adopted from the best-fit Sérsic model of the NIRCam image with GALFIT. From this modeling, we derive a mean lensing magnification factor of $\mu_{\mathrm{S}} = 1.9$ for the southern component, and $\mu_{\mathrm{N}} = 2.7$ for the northern component. The mean lensing magnification for HDF850.1 is $\bar{\mu} = 2.5$, which is slightly larger those assumed in Neri et al. (2014), Serjeant & Marchetti (2014; in the latter case based on the positions of the [C II] emission). The magnification factor is corrected in the following section when we discuss the intrinsic physical properties of HDF850.1.

3.3. Physical Model of SED

We carry out physical SED modeling of HDF850.1 using two software versions, CIGALE (Noll et al. 2009; Boquien et al. 2019, as fiducial results) and BAGPIPES (Carnall et al. 2018, for comparison). Both approaches assume energy balance in dust absorption and emission. For CIGALE modeling, we assume a commonly used delayed-τ star formation history (SFH), in which $\mathrm{SFR}(t) \propto t \exp(-t/\tau)$ and τ is the peak time of SF. An optional late starburst is allowed in the last 20 Myr. We use Bruzual & Charlot (2003) stellar population synthesis models. We also allow a metallicity range of $0.2Z_{\odot} - Z_{\odot}$, and a broad ionization parameter ($\log U$) range of -1 to -3.5. We adopt a modified Calzetti et al. (2000) attenuation curve, allowing the variation of the power-law slope by ± 0.3, and also the dust emission model of Draine & Li (2007). Similar parameters are also assumed for BAGPIPES modeling.

We model the SEDs of HDF850.1-N, -S and two components combined. In rest-frame UV–optical bands, we only use the nine-band NIRCam photometry because the galaxy is undetected with HST (the data are shallower) and heavily blended with foreground sources in the Spitzer/IRAC bands. To avoid invoking unrealistic dust attenuation and IR
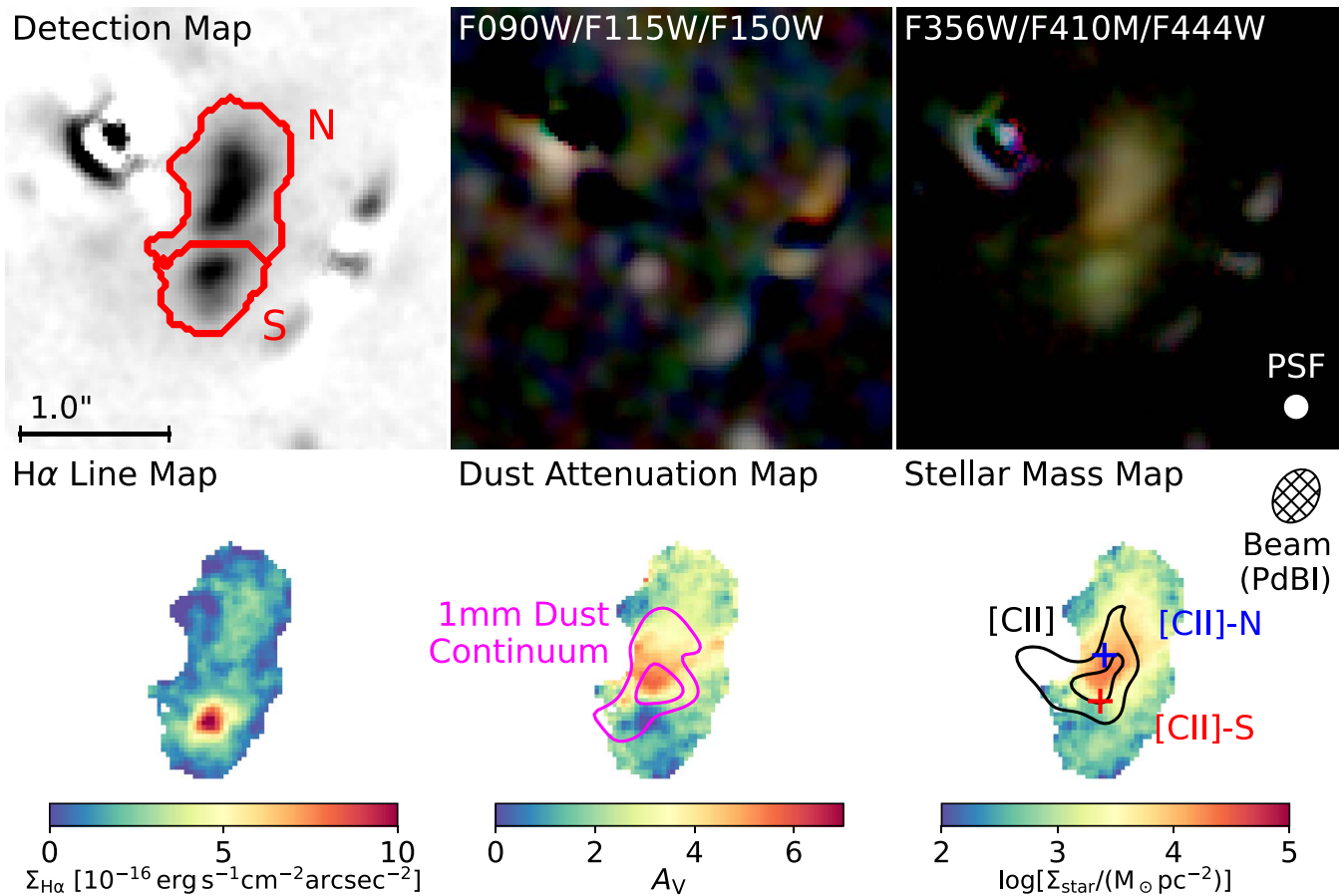
Figure 2. JWST NIRCam images after neighbor subtraction and PSF matching. Image sizes are $3'' \times 3''$ (north up, east left). The FWHM of the matched NIRCam PSF (F444W) is shown in the top right panel. Top left: detection map obtained by stacking the F335M, F356W, F410M, and F444W images. The deblended segments of the HDF850.1-N and -S components are shown in solid red lines. Top center: Rest-frame UV image of HDF850.1 (red, F150W; green, F115W; blue, F090W). The southern component is detected in these images (4σ–9σ). Top right: Rest-frame optical image of HDF850.1 (red, F444W; green, F410M; blue, F356W). The Hα line is within the bandwidths of F410M and F444W filters. The northern component is strongly dust-reddened, and the southern component exhibits bright Hα emission. Bottom left: Hα line map derived from pixelated SED modeling (Section 3.5). The Hα emission from the southern component is higher in terms of surface brightness. Bottom center: Dust-attenuation (A_V) map derived from pixelated SED modeling. The center of HDF850.1 is highly dust-obscured ($A_V \gtrsim 5$), and the high-A_V region matches well with the 1 mm dust continuum emission observed with the PdBI (magenta contours at 4σ and 6σ; Neri et al. 2014). Bottom right: Stellar mass map derived from the A_V and observed F356W (i.e., rest-frame V-band) maps. The integrated intensity map of the [C II] 158 μm line is shown as black contours (4σ and 6σ; Neri et al. 2014). The blue and red plus signs mark the centroids of northern and southern [C II] components in Neri et al. (2014), respectively. The beam size of PdBI observation is indicated in the upper right corner.

luminosity, we also include the Herschel/SPIRE nondetection limits (Walter et al. 2012) in the fitting. Other (sub) millimeter flux densities are not used in the fitting because it is challenging to decompose the dust continuum flux densities from the northern and southern components. The inaccuracy of the energy balance assumption because of patchy dust geometry in contrast to that of the stellar component is also a concern (e.g., see discussions in Kokorev et al. 2021; and evidence in Section 4.3). Far-IR SED modeling of HDF850.1 is presented in Section 3.4. However, we confirm that the inclusion of millimeter photometry does not change our best-fit results with CIGALE presented below, despite a much larger χ^2 of the best-fit SED model.

The best-fit CIGALE SEDs of HDF850.1-N/S and the whole system combined are show in Figure 3. The reduced χ^2 is smaller than 1 for all three fittings, indicating a good fit quality. The best-fit physical parameters are presented in Table 1. We find that the northern component is higher in dust attenuation, stellar mass, and SFR than the southern component, while the nebular emission in the northern component is much fainter (see further pixelated SED modeling presented in Section 3.5).

The best-fit stellar mass and SFR of the whole system are consistent with the combination of best-fit results for the two components. We also find a good agreement between the best-fit results of CIGALE and BAGPIPES.

The intrinsic $B - V$ of the unattenuated stellar continuum of the best-fit SED for HDF850.1 is 0.04, and the best-fit A_V is 4.6 ± 0.7. The intrinsic (lensing-corrected) stellar mass of HDF850.1 is $\log(M_{star}/M_\odot) = 10.8 \pm 0.1$. This is broadly consistent with the stellar mass estimated by Serjeant & Marchetti (2014) with deblended IRAC 5.8 and 8.0 μm flux densities assuming the same IMF. However, we note that the expected IRAC 5.8 and 8.0 μm flux densities from our best-fit SED (1.5 and 3.0 μJy) are somewhat smaller than those reported in Serjeant & Marchetti (2014, 2.7 ± 0.5 and 5.9 ± 0.7 μJy, respectively). The stellar mass that we derived is much larger than the gas mass of 1.6×10^{10} $M_\odot$ found by Neri et al. (2014, updated with new lens model), implying a gas fraction of $f_{gas} = M_{gas}/(M_{star} + M_{gas}) = 0.18 \pm 0.10$, which is lower than the typical gas mass fraction of $z \sim 5$ SMGs reported in Dudzevičiūtė et al. (2020, $f_{gas} \sim 0.55$) but consistent with certain $z = 4$–6 SMGs in literature (e.g., Gómez-Guijarro

Table 1
Summary of the Properties of HDF850.1 at $z = 5.18$

	HDF850.1-N	HDF850.1-S	HDF850.1
R.A. [deg]	189.21655	189.21661	189.21658
Decl. [deg]	62.20723	62.20706	62.20715
Photometric measurements (with 5% noise floor)			
F090W [nJy]	5.0 ± 3.1	10.0 ± 2.3	15.0 ± 3.9
F115W [nJy]	2.8 ± 2.3	13.1 ± 1.8	15.8 ± 2.9
F150W [nJy]	2.0 ± 2.8	19.0 ± 2.2	20.9 ± 3.5
F200W [nJy]	2.5 ± 2.3	31.7 ± 2.3	34.2 ± 3.2
F277W [nJy]	48.7 ± 2.8	95.7 ± 4.9	144.4 ± 5.6
F335M [nJy]	172.2 ± 8.8	85.3 ± 4.4	257.4 ± 9.8
F356W [nJy]	203.0 ± 10.2	99.1 ± 5.0	302.1 ± 11.4
F410M [nJy]	500.5 ± 25.1	266.7 ± 13.4	767.2 ± 28.5
F444W [nJy]	630.9 ± 31.6	242.5 ± 12.2	873.4 ± 33.9
Spectroscopic measurements			
$z_{\rm spec}$	5.179 ± 0.005	5.192 ± 0.001	5.184 ± 0.002
Hα flux [10^{-18} erg s^{-1} cm^{-2}]	7.7 ± 0.2	9.3 ± 0.3	17.7 ± 1.2
Physical properties (corrected for lensing magnification μ)			
μ	2.7	1.9	2.5
$\log[M_{\rm star}/M_\odot]$	10.7 ± 0.4	9.7 ± 0.1	10.8 ± 0.1
$\log[{\rm SFR}_{100\,{\rm Myr}}/M_\odot\,{\rm yr}^{-1}]$	2.1 ± 0.2	1.8 ± 0.1	2.4 ± 0.3
$\log[{\rm SFR}_{\rm UV}/M_\odot\,{\rm yr}^{-1}]$	-1.2 ± 0.2	-0.7 ± 0.1	-0.7 ± 0.1
A_V [mag]	4.9 ± 0.4	4.3 ± 0.1	4.6 ± 0.7
$\log({\rm IRX}) = \log(L_{\rm IR}/L_{\rm UV})$	...	...	3.6 ± 0.2
$\beta_{\rm UV}$	...	-0.44 ± 0.18	-0.77 ± 0.23
$f_{\rm gas} = M_{\rm gas}/(M_{\rm star} + M_{\rm gas})$	...	...	0.18 ± 0.10

Note. Hα line fluxes for HDF850.1-N/S are measured from the Hα line image segments, while the flux for the whole system is measured from the grism spectrum. SFRs derived from SED modeling are averaged over 100 Myr of the most recent star formation history. UV SFRs are derived from the best-fit UV continuum flux densities with conversion factor in Kennicutt & Evans (2012) and are not corrected for dust attenuation.

et al. 2022b; Zavala et al. 2022). We also derived a lensing-corrected $\log[{\rm SFR}/(M_\odot\,{\rm yr}^{-1})] = 2.4 \pm 0.3$.

3.4. Mid-far Infrared Properties

Figure 4 shows the available measurements of the HDF850.1 SED from mid-IR to millimeter, along with two template SEDs. The galaxy is so faint that the confusion noise is an issue for the measurements with Spitzer and Herschel (Dole et al. 2003, 2004; Nguyen et al. 2010; Berta et al. 2011). At 24 μm, we have combined the statistical error with the 1σ photometric criterion confusion noise by the root sum square. In the Herschel bands, significant detections were not achieved, so we show 2σ upper limits from Walter et al. (2012).

Cowie et al. (2009) measured a Spitzer/MIPS 24 μm flux density of 28.2 ± 4.4 μJy for HDF850.1 and treated it as an upper limit because of source confusion. Based on the HST and JWST photometry and SED modeling, we conclude that the $z = 1.224$ foreground elliptical galaxy is quiescent, and therefore, its 24 μm flux density is negligible (~ 1 μJy). However, the lensed arc at $z_{\rm phot} \sim 2.02$ is star-forming (SFR $\sim$ 20 $M_\odot\,{\rm yr}^{-1}$), which could contribute to a 24 μm flux density of ~ 15 μJy according to the LIRG ($L_{\rm IR} = 10^{11}$ $L_\odot$) template in Rieke et al. (2009). Therefore, the 24 μm flux density of HDF850.1 is ~ 13 μJy, consistent with the predicted value from the best-fit CIGALE SED in Section 3.3.

The figure demonstrates that the far-IR measurements only loosely constrain the SED and hence the IR luminosity. As a result, the behavior in this spectral range needs to be determined relative to other galaxies from which reasonably well-constrained templates have been constructed. These issues are discussed in detail in De Rossi et al. (2018), where it is shown that the template of local (U)LIRGs from Rieke et al. (2009) for $\log(L_{\rm IR}/L_\odot) = 11.25$ is well suited for infrared galaxies at $2 \leqslant z < 4$, and a template based on the behavior of Haro 11, with greatly enhanced output in the 20 μm range, is preferred for $5 \leqslant z < 7$. The underlying cause for this shift toward a warmer far-IR SED is the compact size and intense heating of dust by star formation in the high-redshift galaxies, properties potentially shared by HDF850.1.

As shown in Figure 4, the $\log(L_{\rm IR}/L_\odot) = 11.25$ template does a poor job of matching the SED slope of HDF850.1 from 450 μm through the submillimeter and millimeter wave range. As discussed in De Rossi et al. (2018), it is also too cold in the 100–300 μm (observed) range to match theoretical expectations. The Haro 11 based template is too bright in the 100–300 μm range, perhaps because HDF850.1 is at the low-redshift end of the $5 < z < 7$ bin where it was derived. We have generated a new template specifically for the $4 < z \leqslant 5$ range by combining the $\log(L_{\rm IR}/L_\odot) = 12.25$ and Haro 11 templates to fit the measurements in De Rossi et al. (2018). The best fit is with about 65% of the Haro 11 template and 35% of the $\log(L_{\rm IR}/L_\odot) = 12.25$ one. This template closely resembles the one proposed for this redshift by Schreiber et al. (2018), although it provides a somewhat better fit even than that one. The new template is shown in Figure 4 to fit the data for HDF850.1 well, although it is clearly not unique. We note that
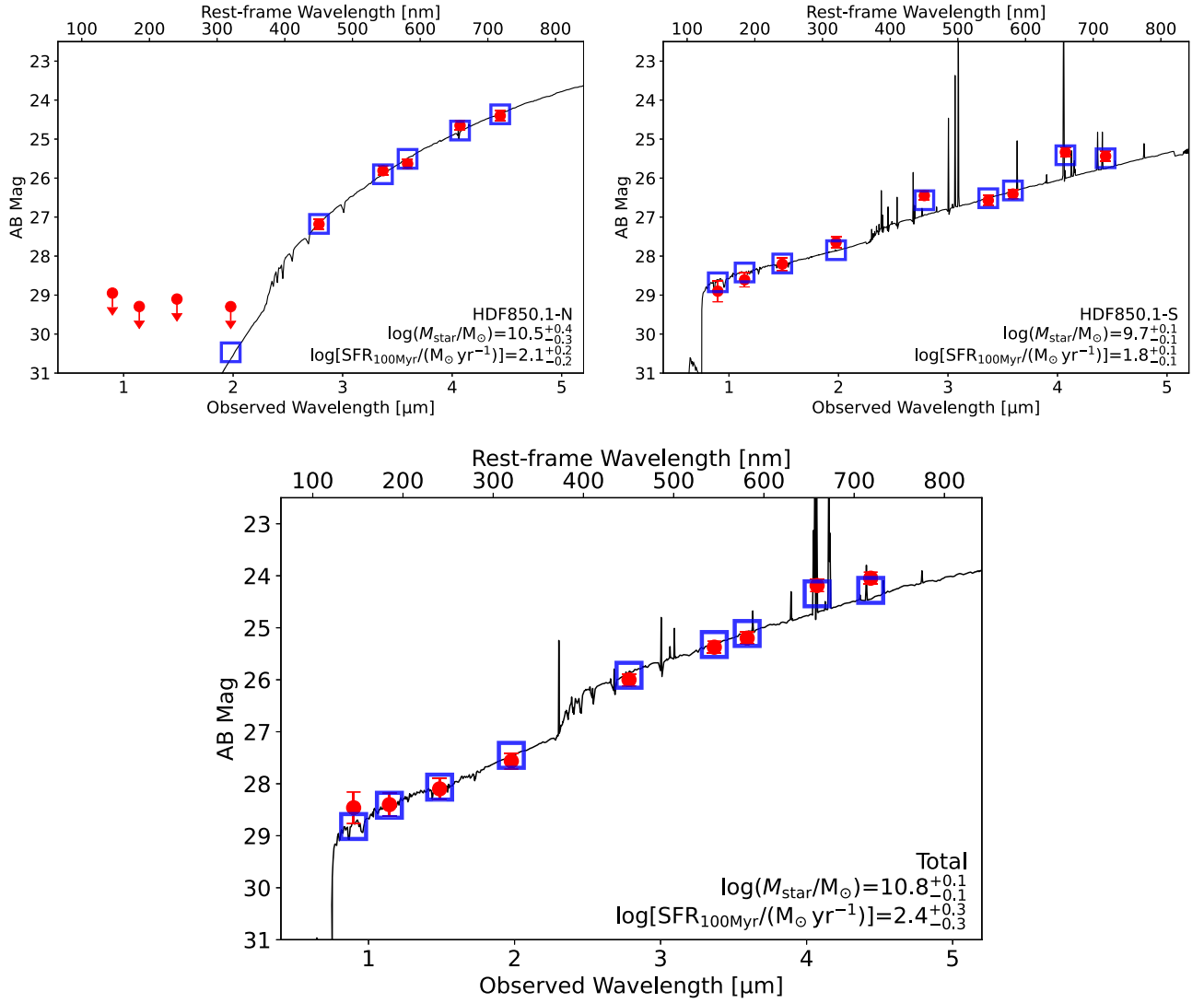
Figure 3. Best-fit CIGALE SED models of HDF850.1-N (top left), HDF850.1-S (top right), and the whole system (bottom). JWST/NIRCam photometric measurements are shown as red circles, and best-fit source flux densities are shown as open blue squares. Best-fit source properties have been corrected for lensing magnification (Section 3.2).

the template overpredicts the 2–3 mm flux densities, which is caused by the large dust emissivity index ($\beta \sim 2.5$) of HDF850.1 as pointed out in Walter et al. (2012).

In Figure 4, we also show the far-IR SED of the exceptionally bright lensed galaxy HLS J091828.6+514223 (HLSJ0918) at $z = 5.24$ (Combes et al. 2012; Rawle et al. 2014). The intrinsic IR luminosity of this galaxy is $1.8 \times 10^{13}\, L_\odot$, a factor of ~ 3 larger than that of HDF850.1, but because of a lensing magnification of ~ 9, the peak of the far-IR SED reaches 212 mJy at 500 μm, producing high S/N detections in all three SPIRE bands and providing a tight constraint on the far-IR SED shape around the peak. The figure shows that the measured far-IR SED of HLSJ0918 is broadly consistent with that of HDF850.1 and the newly derived warm SED template.

The indicated IR luminosity of HDF850.1 is $\sim 1.2 \times 10^{13} \mu^{-1} L_\odot$ before lensing correction. Corrected for the lensing magnification, the intrinsic $L_{\rm IR}$ is $\sim 5 \times 10^{12}\, L_\odot$. The potential systematic errors dominate the uncertainty in this value, and could be as much as $2 \times 10^{12}\, L_\odot$. In comparison, Walter et al. (2012), Serjeant & Marchetti (2014) estimated values of

$(8.7 \pm 1) \times 10^{12}$ and $1 \times 10^{13} \mu^{-1} L_\odot$, the former value $\sim 70\%$ of our value uncorrected for lensing. This difference is a direct result of their using templates that are weak in the mid-IR compared with the typical behavior of ULIRGs at similar redshift (De Rossi et al. 2018).

Applying the relation between total IR luminosity and the SFR from Kennicutt & Evans (2012) would lead to an SFR estimate of $700 \pm 300\, M_\odot\, {\rm yr}^{-1}$. This value is substantially larger than the $\sim 270 \pm 130\, M_\odot\, {\rm yr}^{-1}$ estimated by modeling the rest wavelength UV–optical spectrum in the preceding section. The difference is not surprising given the very large extinction and the resulting possibility that a significant part of the ongoing star formation is deeply hidden at those wavelengths.

3.5. Maps of Hα Line and Stellar Continuum

We also perform a pixel-by-pixel modeling of the SED of HDF850.1 in the LW filters. We assume a simple power-law continuum model and a delta function at 4.06 μm for the Hα emission line at $z = 5.185$. This also effectively assumes negligible [N II] $\lambda\lambda$ 6548, 6583 and [S II] $\lambda\lambda$ 6716, 6731
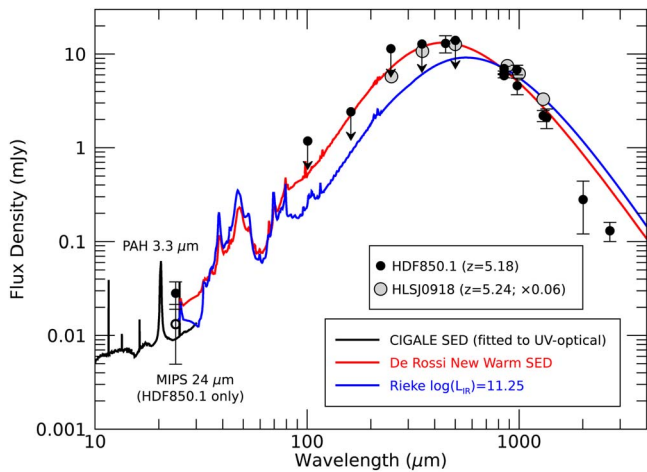
Figure 4. Far-IR (rest-frame) photometry of HDF850.1. The measurements are from Cowie et al. (2009; 24 μm; the empty circle shows the HDF850.1-only flux density of 13 μJy), Walter et al. (2012; 100–500 μm and 0.98/2.7 mm), Cowie et al. (2017; 450 μm), Hughes et al. (1998; 850 μm, 1.35 mm), Chapin et al. (2009; 850 μm; the measurement at 1.1 mm is not plotted because of its low signal to noise), Neri et al. (2014; 980 μm), Downes et al. (1999; 1.3 mm), and Staguhn et al. (2014; 2 mm). The SED templates (scaled to the 850 μm points) are from Rieke et al. (2009; blue line) and the newly derived warm SED template preferred for the redshift of HDF850.1 (red line). The latter is broadly consistent with the measured SED shape of the bright lensed galaxy HLSJ0918 at $z = 5.24$ (Rawle et al. 2014). The 24 μm points have an error bar determined by combining the statistical error and expected confusion noise by root sum square; for the 100, 160, 250, 350, and 500 μm points, the 2σ upper limits from Walter et al. (2012) are shown. The best-fit CIGALE SED for the whole system is also plotted up to 30 μm (black line). Please refer to Walter et al. (2012) for a far-IR SED model fit based on a modified blackbody using the MAGPHYS program (da Cunha et al. 2008).

emission ($\lesssim 10\%$ of Hα; see Section 3.7). The Hα line is within the bandwidths of F410M and F444W filters.

From the best-fit models, we derive the Hα emission-line map as shown as the bottom left panel of Figure 2. The southern component is higher in Hα surface brightness, while the Hα emission from the northern component is more diffuse and lower in surface brightness. The total Hα line flux integrated from the image segments is $(1.7 \pm 0.1) \times 10^{-17}$ erg s^{-1} cm^{-2}, where the uncertainty is computed from the error extension of the best-fit Hα line map. We find that ~55% of the Hα flux is from the southern component.

The best-fit slope of the underlying continuum reflects the rest-frame optical color indices (e.g., $B - V$) of HDF850.1 in a spatially resolved manner. Under the assumption that (i) the stellar population within the galaxy is homogeneous with a common intrinsic $B - V$ of 0.04 ± 0.20 (based on the physical SED modeling in Section 3.3), and (ii) the dust attenuation follows the Calzetti et al. (2000) law, we convert the map of rest-frame optical continuum slope into a dust-attenuation map (A_V; bottom-center of Figure 2). The highest dust attenuation ($A_V > 5$) is observed around the southern tip of HDF850.1-N, which is clearly seen reddened in the F444W − F410M − F356W red giant branch (RGB) image. This highly dust-attenuated region is also spatially consistent with the 1 mm dust continuum emission obtained with the PdBI (Neri et al. 2014). The lowest dust attenuation ($A_V < 1$) is seen in HDF850.1-S, exactly at the location of the compact clump seen in rest-frame UV. It is worth reminding that rest-frame UV data are not used in this simple SED modeling.

Combining the A_V map and the rest-frame V-band image observed with the F356W filter, we are able to reconstruct a rest-

frame V-band image of HDF850.1 that is free from dust attenuation (Figure 2, bottom right panel). Under our previous assumption of a homogeneous stellar population, this is effectively a map of the stellar mass distribution. The total stellar mass derived from this map is consistent with that derived from integrated physical SED modeling (Section 3.3) assuming the same mass-to-light ratio. We also find that the stellar mass can be well described by one component instead of two components as seen in the LW detection map. The stellar mass centroid is also on the southern tip of HDF850.1-N, consistent with the region with highest dust attenuation, suggesting that HDF850.1 is split into two components at rest-frame optical wavelength because of heavy dust obscuration in the center. The stellar mass distribution is also broadly consistent with the [C II] 158 μm intensity map (i.e., moment 0) obtained by Neri et al. (2014), although the [C II] emission shows signs of extension toward the $z = 1.224$ elliptical galaxy. This region is subject to the residual of neighbor subtraction in our NIRCam images, and no stellar continuum can be robustly detected.

We also experiment pixel-by-pixel physical SED modeling of HDF850.1 with the same software and assumption as that in Section 3.3 (similar to those performed in recent JWST studies including Giménez-Arteaga et al. 2023; Pérez-González et al. 2023). The patterns of stellar mass and dust-attenuation map are similar to those presented in Figure 2 derived with a simple power law and a delta function model. However, we observe a clear degeneracy between the best-fit stellar age and A_V for each pixel, and the vast majority of pixels can be modeled with a mass-weighted stellar age of ~100 Myr except for the UV-bright, Hα-emitting region of HDF850.1-S (~30 Myr). This is because our current data set does not cover the rest-frame J band for HDF850.1, and most of the pixels are not detected in the rest-frame U band. It is therefore very difficult to obtain spatially resolved diagnostics of stellar population and A_V at the same time for HDF850.1 on a pixel-to-pixel level with the current data set. Therefore, we opt not to report the physical parameters of HDF850.1 obtained through this method.

3.6. Size of HDF850.1

We measure the size of HDF850.1 in the image plane at rest-frame V band with and without dust-attenuation correction. Through a simple 2D Gaussian fitting to the stellar mass map derived in Section 3.5, we obtain a half-mass–radius of HDF850.1 along the major axis as $R_e = 0\farcs27 \pm 0\farcs02$. We also model the map with 2D Sérsic profile using GALFIT (Peng et al. 2010), and we find $R_e = 0\farcs21 \pm 0\farcs02$, with best-fit Sérsic index $n = 1.3 \pm 0.1$. Both effective radii have been deconvolved with the PSF.

To account for the irregular shape of HDF850.1 and the uncertainty of the dust-attenuation modeling, we also measure the size from the 1D profile of HDF850.1 along its major axis. We use a set of elliptical annulus apertures from the mass centroid of HDF850.1 with $b/a = 0.54$, and constant annulus width of $\Delta r = 0\farcs06$. We also perform Monte Carlo simulations of the stellar-mass map, which considers the uncertainty from photometry, intrinsic $B - V$, and dust attenuation. We then derive the uncertainty of the 1D mass profile from the standard deviation of the profiles measured with these simulations. The radial mass profile of HDF850.1 is shown as the filled red circles and solid line in Figure 5. In comparison, we also show the 1D profile of ePSF and rest-frame V-band (F356W) light in the same figure. The half-mass–radius derived from 1D profile
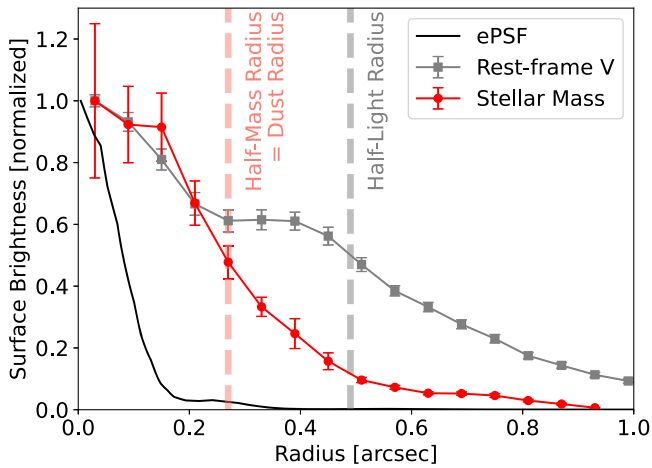
Figure 5. 1D profile of HDF850.1 along the direction of major axis in the image plane. Surface brightness profile in the rest-frame *V* band (F356W) is shown in gray, and stellar mass profile (Section 3.5) is shown in red. Half-light and half-mass radii are highlighted as vertical dashed lines. The half-mass–radius is consistent with the half-light radius of 1 mm dust continuum measured by Neri et al. (2014). Empirical PSF profile in the F444W band is shown in solid black line for comparison. All profiles are normalized to 1 at the centroids.

is $0\overset{''}{.}27 \pm 0\overset{''}{.}02$ after PSF deconvolution. This is much smaller than the half-light radius in rest-frame *V* band ($0\overset{''}{.}49 \pm 0\overset{''}{.}02$). The smaller half-mass–radius in contrast to half-light radius is a natural consequence of higher dust attenuation in the galaxy center, which flattens out the rest-frame optical light profile (e.g., Nelson et al. 2016; Mosleh et al. 2017; Tacchella et al. 2018; Lang et al. 2019; Chen et al. 2022; Cheng et al. 2022, 2023; Suess et al. 2022; Wu et al. 2023).

3.7. Hα Spectroscopy of HDF850.1

We extract the NIRCam grism spectrum of HDF850.1 at 3.9–4.8 μm obtained through the FRESCO program (Oesch et al. 2023). The spectrum was obtained with Module B of NIRCam, and the dispersion direction is 40° from the north in clockwise direction. The most notable feature in the spectrum is the Hα emission (Figure 6; for completeness, the full spectrum of HDF850.1 is displayed in Appendix, Figure A3). The 2D grism spectrum of HDF850.1 reveals similar Hα morphology as that derived with the NIRCam images (Section 3.5), including bright and compact Hα emission from the southern component and diffuse emission from the northern component. The Hα redshift of the whole system is $z = 5.184 \pm 0.002$ in extracted 1D spectrum, consistent with the [C II] redshift ($z_{[C\ II]} = 5.185$) reported in Neri et al. (2014). The total Hα flux measured from the grism spectrum is $(1.8 \pm 0.1) \times 10^{-17}$ erg s^{-1} cm^{-2}, consistent with that derived from NIRCam image. [N II] lines are not detected, which is likely a combined result of (i) blending with Hα emission because the NIRCam WFSS resolution decreases for extended sources, and (ii) a low [N II]/Hα line ratio ($\lesssim 10\%$) as seen for $z > 5$ galaxies reported in recent NIRSpec and NIRCam grism studies (e.g., Cameron et al. 2023; Helton et al. 2023; Sanders et al. 2023; Shapley et al. 2023).

The NIRCam grism spectrum also resolves the kinematics of HDF850.1. The best-fit Hα redshift for HDF850.1-S is $z = 5.192 \pm 0.001$, indicating a velocity offset of $\Delta v = 330 \pm 70$ km s^{-1} from the galaxy center where the redshift is measured through the [C II] line. The Hα emission of HDF850.1-N is likely blueshifted ($z = 5.179 \pm 0.005$) when

compared with the galaxy center, although the velocity offset ($\Delta v = -310 \pm 240$ km s^{-1}) is much more uncertain because of the low surface brightness. The kinematic information derived from the NIRCam grism is broadly consistent with that from the [C II] observations presented in Neri et al. (2014).

4. The Nature of HDF850.1

4.1. SFR versus Stellar and Gas Mass

The left panel of Figure 7 compares the SFR and stellar mass of HDF850.1 with massive star-forming galaxies at $z = 4$–6 observed through the ALMA large program ALPINE (Béthermin et al. 2020; Le Fèvre et al. 2020), and also the so-called star-forming main sequence at $z = 5$ (Speagle et al. 2014; Schreiber et al. 2015; Popesso et al. 2023). Here, we adopt the SFR derived from the mid-to-far-IR SED modeling.

As one of the most massive galaxies found in the $z > 5$ Universe, the SFR of HDF850.1 is slightly above that expected from the star-forming main sequence. We note that $z > 5$ galaxies with similar stellar mass are rare with regard to volume density ($\lesssim 10^{-5}$ cMpc^{-3} dex^{-1}; e.g., Weaver et al. 2023), and thus, such a mass and redshift parameter space can be underweighted for the determination of star-forming main sequence across cosmic time. The high dust attenuation, high obscured fraction of SFR (SFR$_{UV}$/SFR$_{total} < 10^{-3}$ for HDF850.1), and high incompleteness in spectroscopic confirmation and (sub) millimeter SED constraints make the main-sequence SFR of such galaxies even more uncertain before the era of the JWST. If the star-forming main sequence does exist at $z \gtrsim 5$ and $M_{star} \sim 10^{11}$ $M_\odot$, given the accurate JWST photometry and stellar SED modeling, HDF850.1 could be an example of a galaxy that anchors the massive end of such a main sequence at $z \gtrsim 5$ (see also Serjeant & Marchetti 2014).

With the IR-based SFR and molecular gas mass measured by Neri et al. (2014), the molecular gas depletion time is only $t_{dep} = M_{gas}/SFR = 25^{+25}_{-15}$ Myr (60^{+70}_{-35} Myr if we adopt the SFR from NIRCam SED fitting). Both short timescales indicate that HDF850.1 will likely quench at $z \simeq 4.7$–5.0 if there is no further molecular gas replenishment (see the massive quiescent galaxy at $z = 4.658$ confirmed with Carnall et al. 2023).

4.2. HDF850.1 Is Not Necessarily a Major Merger

With $0\overset{''}{.}3$ resolution PdBI observation of the [C II] 158 μm line of HDF850.1, Neri et al. (2014) found two components of [C II] emission with distinct velocity and spatial offsets (330 km s^{-1} and $0\overset{''}{.}3$, respectively). A number of physical properties of HDF850.1 are similar to those of major-merger ULIRGs in the local Universe (e.g., Arp 220), including IR luminosity, CO line luminosities, and strong dust obscuration. Together with other arguments including the irregular shape of the [C II] moment 0 map (Figure 2, bottom right panel), Neri et al. (2014) concluded that HDF850.1 is a galaxy merger.

With the latest JWST observation of HDF850.1 and other studies of high-redshift ($z \gtrsim 5$) star-forming galaxies over the past decade, we argue that HDF850.1 is not necessarily a major-merger system, but our observations cannot rule out the potential existence of a minor merger component, especially given the overdense environment at $z \sim 5.2$ (see Section 5). Indeed, one can speculate that the southern component is an infalling galaxy that is lower in dust-attenuation than the center of HDF850.1 (or simply the northern component), but the stellar mass ratio between HDF850.1-S and -N ($\lesssim 1/10$) is
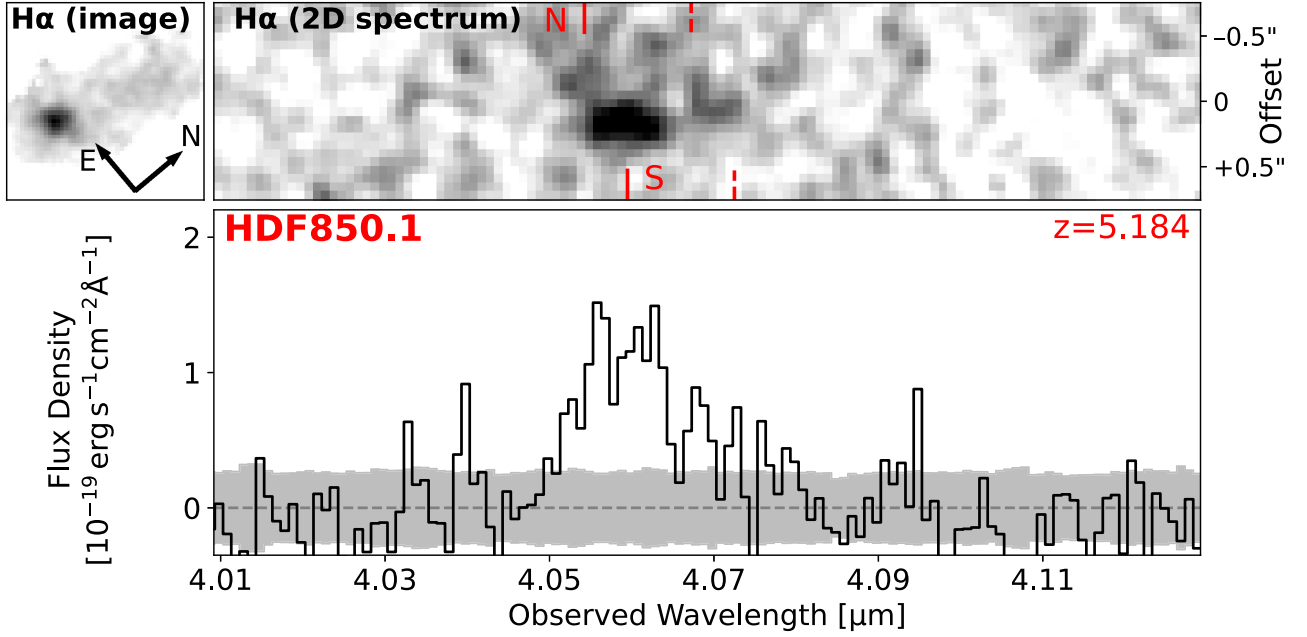
Figure 6. NIRCam grism spectrum of HDF850.1 obtained from FRESCO. Top left: same Hα emission-line map as in Figure 2, but rotated to align with the dispersion direction. Top right: 2D grism spectrum of HDF850.1. Hα line emissions from the northern and southern components are indicated with solid vertical red lines, and expected [N II] $\lambda6583$ line emissions are indicated by dashed lines. The relative positions of Hα emission from HDF850.1-N and S are different from those in the top left panel, suggesting different velocities of the two components. Bottom: 1D spectrum of HDF850.1 obtained by collapsing the 2D spectrum within $\pm0\rlap{.}''5$ spatial offset. The uncertainty spectrum is shown as the filled gray region. The full 1D spectrum is displayed in Appendix, Figure A3.
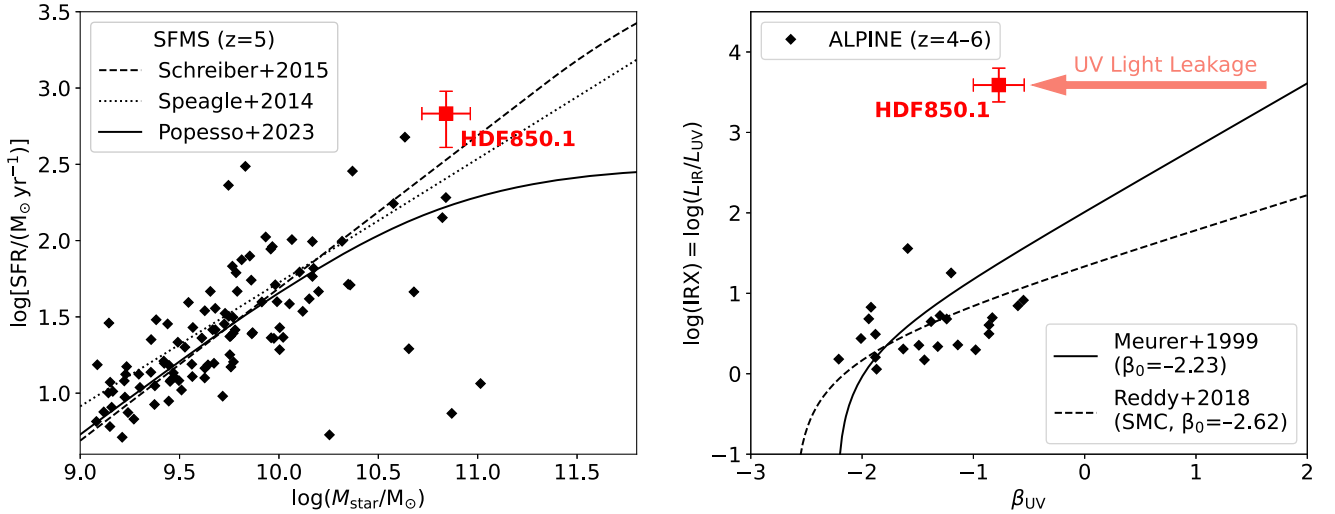

Figure 7. Left: star formation rate vs. stellar mass of HDF850.1 (red square), compared with $z = 4$–6 galaxies observed with the ALMA ALPINE survey (Béthermin et al. 2020; Le Fèvre et al. 2020). The best-fit star-forming main sequences at $z = 5$ in Speagle et al. (2014), Schreiber et al. (2015), and Popesso et al. (2023) are also plotted for comparison. Right: infrared excess vs. UV continuum slope of HDF850.1, compared with $z = 4$–6 galaxies in the ALPINE sample whose dust continua are detected with ALMA (Fudamoto et al. 2020). IRX–$\beta_{\rm UV}$ relations of Meurer et al. (1999), Reddy et al. (2018) are also plotted for comparison. HDF850.1 is well above (or bluer than) these relations because of inhomogeneous dust attenuation and leakage of UV light in the southern component.

lower than the canonical threshold of $1/4$ that differentiates minor and major mergers.

Despite the two-component morphology seen in the deblended rest-frame optical image, we found excellent spatial agreement between the dust-attenuation and dust emission map in Section 3.5, which suggests that the gap between the two components results from a high amount of dust attenuation. The derived stellar mass map is also well described with a single component model, indicating that it is not necessary to include a secondary galaxy component for the interpretation.

After a decade of ALMA operation at subarcsec resolution (see a recent review by Hodge & da Cunha 2020), it is now known that in the high-redshift Universe, luminous SMGs are not necessarily major mergers in the final coalescence phase. Minor mergers and secular evolution can be important trigger mechanisms for vigorous dusty starbursts at $z \gtrsim 2$ (e.g., Fujimoto et al. 2017; Gómez-Guijarro et al. 2018; Rujopakarn et al. 2019; Sun et al. 2021b). This has been recently confirmed with JWST rest-frame optical observations (e.g., Chen et al. 2022; Cheng et al. 2022, 2023; Le Bail et al. 2023; Rujopakarn

et al. 2023), in which SMGs are often observed as fairly isolated disks (with or without noticeable substructures), and some of them exhibit spiral-arm features that could be triggered as a result of minor mergers (e.g., Wu et al. 2023). This is different from the local ULIRGs that are predominantly gas-rich major mergers (e.g., Sanders et al. 1988). Therefore, the similarity between HDF850.1 and local ULIRGS in physical properties (luminosity and dust obscuration) is not a strong argument to justify a major-merger interpretation for HDF850.1.

However, the [C II] morphology and kinematics could favor a major-merger scenario as pointed out by Neri et al. (2014). Alternatively, the [C II] emission may be a tracer of gas outflow (e.g., Cicone et al. 2015; Maiolino et al. 2015; Ginolfi et al. 2020; Pizzati et al. 2020; Herrera-Camus et al. 2021; Akins et al. 2022), which could extend out to a $\sim$10 kpc scale, as in [C II] halos (e.g., Fujimoto et al. 2019, 2020; Lambert et al. 2023; Pizzati et al. 2023). The outflow direction can differ from the major axis of the galaxy (e.g., HZ4 at $z = 5.5$; Herrera-Camus et al. 2021), which is the case for HDF850.1 where the [C II] extends toward the $z = 1.224$ elliptical galaxy. The [C II] extension of HDF850.1 is closer to the lensing critical curve and magnified by a higher factor ($\mu \sim 5$), making it easier to detect.

The broad [C II] and CO line widths (total [C II] width $\sim$940 km s^{-1}; Neri et al. 2014) do not necessarily require an interpretation as a major merger. Walter et al. (2012) derived a dynamical mass of $M_{\rm dyn} \sim 1.3 \times 10^{11}\ M_{\odot}$ (lensing-uncorrected) through the far-IR line widths and a simple rotating disk assumption with an inclination of 30°. Indeed, the blueshifted and redshifted [C II] components in Neri et al. (2014) peak at opposite directions from the newly determined stellar-mass centroid (Figure 2), favoring a rotation disk interpretation. With the half-mass–radius of $\sim$1.0 kpc in the source-plane, an inclination of $\sim$55° from the axis ratio of stellar mass distribution (assuming a thin circular disk), and also the velocity dispersion from [C II] and Hα lines ($\sigma_V \sim 300$ km s^{-1}), we estimate a dynamic mass of $M_{\rm dyn} \sim 8 \times 10^{10}\ M_{\odot}$ for the whole HDF850.1 system following the method adopted by Daddi et al. (2010), Walter et al. (2012). This is actually consistent with the total baryonic mass if we include both our stellar mass estimate and the gas mass measured by Neri et al. (2014). A major-merger interpretation could imply a lower dynamical mass, potentially resulting in tension with the total baryonic mass of the system. It is also worth noticing that the reconcilability between baryonic and dynamic mass of HDF850.1 does not require the use of very top-heavy IMF (e.g., Steinhardt et al. 2023; Woodrum et al. 2023) suggested for the interpretation of luminous $z \gtrsim 8$ galaxies.

Combining all evidence presented above, we conclude that HDF850.1 is not necessarily a major-merger system in the coalescence phase. However, our observations cannot rule out the potential existence of a minor merger component or a major merger in the previous formation history of HDF850.1.

4.3. Leakage of UV and Hα Photons

The southern component of HDF850.1 is detected in the rest-frame UV bands as a compact source, and our spatially resolved dust-attenuation analysis also suggests low attenuation ($A_V < 1$) at the location of the UV source (Section 3.5). Hα emission is also detected at this location. This is in great contrast to the centroid of HDF850.1 with high dust attenuation ($A_V \gtrsim 5$).

The right panel of Figure 7 shows the infrared excess ($\log(\rm IRX) = \log(L_{\rm IR}/L_{\rm UV})$) versus UV continuum slope $\beta_{\rm UV}$ of HDF850.1, which is further compared with the ALPINE sample of $z = 4$–6 galaxies whose dust continua are detected with ALMA (Fudamoto et al. 2020). Here, the $\beta_{\rm UV}$ of HDF850.1 is derived from a simple power-law fitting of four-band SW photometry (F090W $-$ F200W), and the UV luminosity $L_{\rm UV}$ is derived as νL_{ν} at rest-frame 1500 Å. Assuming an intrinsic UV continuum slope of β_0, uniform dust screen, and energy balance of dust absorption and emission, IRX will increase monotonically with the reddening of $\beta_{\rm UV}$ depending on the dust extinction law. The best-fit IRX–$\beta_{\rm UV}$ relation of local starburst galaxies in Meurer et al. (1999) and the SMC relation with a blue $\beta_0 = -2.62$ (Reddy et al. 2018) are plotted for comparison.

In contrast to galaxies in the ALPINE sample that generally follow the SMC-like IRX–$\beta_{\rm UV}$ relation, the IRX of HDF850.1 is $\sim$100 times above the empirical relations at its $\beta_{\rm UV}$. Previous studies have shown that SMGs can host relatively blue UV continuum slopes at large IRX (e.g., Penner et al. 2012; Oteo et al. 2013; Casey et al. 2014). Theoretical works interpret these results through patchy dust screen models, resulting in a decrease in the far-UV optical depth compared with that at optical wavelengths, and also the turbulence of the dust screen (e.g., Popping et al. 2017; Narayanan et al. 2018). With the high-resolution NIRCam images at rest-frame UV, we confirm that the bluer-than-expected $\beta_{\rm UV}$ of HDF850.1 is caused by inhomogeneous dust attenuation and therefore leakage of UV photons.

4.4. The Assembly of the Stellar and Dust Profiles

In the source plane, the half-mass–radius of HDF850.1 is measured as 1.0 ± 0.1 kpc. We note that, in our resolved SED modeling, we assume a constant intrinsic $B - V$ for the stellar population at each pixel, which can be an oversimplified assumption as the spatial variation of stellar age and color index has been observed with JWST for galaxies across $z = 2$–8 (e.g., Miller et al. 2022; Chen et al. 2023; Duncan et al. 2023). Even though we have assumed an intrinsic scattering of $B - V$ of 0.2 mag and taken that into account through Monte Carlo simulations, the derived map of stellar mass can still be biased if an intrinsic color gradient exists for such massive star-forming galaxies, especially when most of the dust-obscured star formation occurs around the galaxy centers. If the center of HDF850.1 is younger than its outskirts and intrinsically bluer, we will then underestimate the dust attenuation in the center, and therefore, the underlying stellar mass distribution could be even more compact.

Despite the potential bias in half-mass–radius estimate, we find that the half-mass–radius of HDF850.1 is broadly consistent with the half-mass radii of massive HST-dark galaxies found with the CEERS sample at similar redshift (Pérez-González et al. 2023; Figure 8). The half-mass–radius of HDF850.1 is slightly smaller than the half-light radius of the CEERS HST-dark galaxies at similar mass and redshift measured in the F444W band (Nelson et al. 2023, $R_e \sim$ 2 kpc), which is likely a result of increasing dust attenuation in the galaxy center and flattening of the rest-frame optical light profile. We also extrapolate the relation between half-mass radii and stellar masses of star-forming galaxies at $z = 2.0$–2.5 (Suess et al. 2019), to $z = 5$ assuming a redshift dependence of $R_{\rm e,mass} \propto (1 + z)^{-1}$ (e.g., Oesch et al. 2010; Shibuya et al. 2015), and we conclude that the size–mass of HDF850.1 is
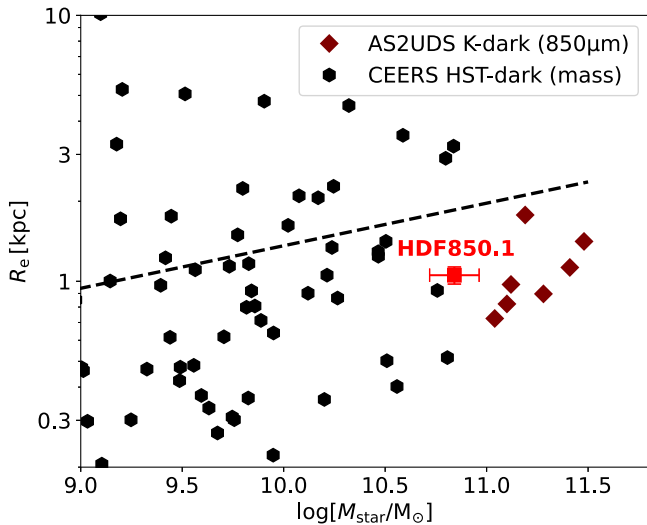
Figure 8. Half-mass–radius vs. stellar mass of HDF850.1 (red square), compared with those of HST-dark galaxies at $z \sim 4.4$ selected from the CEERS JWST program (black hexagons, Pérez-González et al. 2023). The K-dark SMGs at $z \sim 3.4$ in AS2UDS sample are also shown as maroon diamonds for comparison, with their sizes measured at $850\,\mu m$ (i.e., dust continuum; Gullberg et al. 2019; Smail et al. 2021). The dashed line denotes the relation between half-mass radii and stellar masses of star-forming galaxies at $z = 2.0$–2.5 (Suess et al. 2019), but scaled to $z = 5$ assuming the ratio of scale factors of $(1 + z)^{-1}$ at the two redshifts.

consistent with such an extrapolated relation within a dispersion of 0.2 dex.

It is interesting that the dust continuum radius of HDF850.1 measured by Neri et al. (2014) is consistent with the half-mass–radius derived in this paper. Smail et al. (2021) studied K-faint SMGs in the AS2UDS sample (Dudzevičiūtė et al. 2020) with similar stellar mass at $z \sim 3.5$, and found a median effective radius of their dust continuum emission of $\sim 1.0\,kpc$, which is also consistent with the half-mass–radius of HDF850.1. The similar compactness of the stellar and dust components of HST-dark SMGs at high redshift is likely the cause of the high dust attenuation seen in this type of galaxy (median $A_V = 5.2$ in the sample of Smail et al. 2021; and 4.6 ± 0.7 in this work) as suggested by previous studies (e.g., Smail et al. 2021; Sun et al. 2021a).

5. The Environment of HDF850.1

5.1. Hα-emitting Galaxies at Similar Redshifts

HDF850.1 is known to reside in an overdense environment at $z \sim 5.2$, which has been confirmed with ground-based Lyα spectroscopy (Walter et al. 2012; Calvi et al. 2021, 2023). Before the launch of the JWST, these works reported 22 spectroscopically confirmed galaxies within the overdensity, including a known quasar at $z = 5.186$ (Barger et al. 2002). To better understand the environment of HDF850.1, we follow a method similar to that described in Helton et al. (2023) to identify Hα-emitting galaxies at $z = 5.1$–5.5, where the Hα emission is within the bandwidth of F410M and F444W filters, resulting in F410M flux excess.

Similar to Tacchella et al. (2023), we start from the full JADES photometric catalog in the GOODS-N field (B. Robertson et al. 2023, in preparation). We conduct circular aperture photometry at 0.4–5.0 μm (obtained with HST/ACS and JWST/NIRCam) with diameters of $0{.}''2$ and point-source

aperture correction factors. Although the flux densities of extended sources can be underestimated, the color information at the centroids of galaxies is preserved, and therefore, the following photometric redshift analysis is not affected. We use the code EAZY (Brammer et al. 2008), which estimates photometric redshifts using a template-fitting approach. The templates and parameters being used in this step are the same as those described in Helton et al. (2023), Hainline et al. (2023). We select sources with F444W < 29 AB mag, $z_{phot} > 4$ and $\Delta z_{phot} < 1$ for FRESCO grism spectrum extraction, where the EAZY confidence interval (Δz_{phot}) is defined to be the difference between the 16th and 84th percentiles of the photometric redshift posterior distribution. We caution that the accuracy of z_{phot} estimate can be degraded for intrinsically red sources (e.g., SMGs) because of the use of small apertures and SED templates best suited for the selection of $z > 8$ galaxies (Hainline et al. 2023), and therefore, our survey completeness is expected to decrease toward the galaxy population with higher dust attenuation.

For a total of ~ 4000 galaxies that satisfy our selection criteria, we extract 2D grism spectra and collapse them into 1D spectra using a boxcar aperture with a height of five NIRCam LW native pixels (total of $0{.}''31$). We then perform automatic emission-line identification with the 1D spectra, finding peaks at $S/N \geqslant 5$ with various wavelength bin sizes (1–8 nm; corresponding to $\Delta v = 60$–600 km s^{-1}). Here, the noise is measured from the covariance matrix of a Gaussian-profile fitting using 1D scientific and noise spectra.

Similar to Helton et al. (2023), we tentatively assign an emission-line solution (Hα or [O III]) to each of the detected peaks that minimizes the difference between the estimated photometric redshifts and proposed spectroscopic redshifts. Based on our visual inspection, the misidentification of Hα emitters as [O III] emitters at higher redshifts is very rare (<1%). This is because Hα emitters at $z \sim 5.2$ typically also have strong [O III] lines in the F277W band, and thus, the color excess has filters consecutive in wavelength space (e.g., F200W and F335M), resulting in a very tight photometric redshift constraint. We then perform visual inspection on these solutions to remove spurious detections caused by either noise or contamination, and revise misidentifications for a few cases. After this step, we also optimally reextract 1D spectra of confirmed sources using their F444W surface brightness profiles (Horne 1986), which recovers more of the Hα line fluxes for extended sources than those from boxcar extraction. We fit the extracted 1D spectra with Gaussian profiles to measure the redshifts and fluxes. For sources with blended Hα emission in grism data, we fit multiple Gaussian profiles to decompose the fluxes and measure the redshifts properly. The typical redshift uncertainty is $\Delta z = 0.001$, and the typical 5σ detection limit of Hα line is 2×10^{-18} erg s^{-1} cm^{-2}, similar to that reported in Helton et al. (2023) for Hα emitters in the GOODS-S field.

We confirm 146 Hα-emitting galaxies at $z = 5.1$–5.5 with $\geqslant 5\sigma$ detections of Hα lines from the FRESCO spectra, including HDF850.1 itself. The 16th, 50th, and 84th percentiles of the difference between photometric and spectroscopic redshifts ($z_{phot} - z_{spec}$) are -0.04, 0.01, and 0.09, respectively. Figure 9 shows the on-sky distribution of these 146 galaxies overlaid on the footprint of JADES and FRESCO, including 109 galaxies at $z = 5.17$–5.30. We present the NIRCam cutout images and grism spectra of these galaxies in Figure A1 of
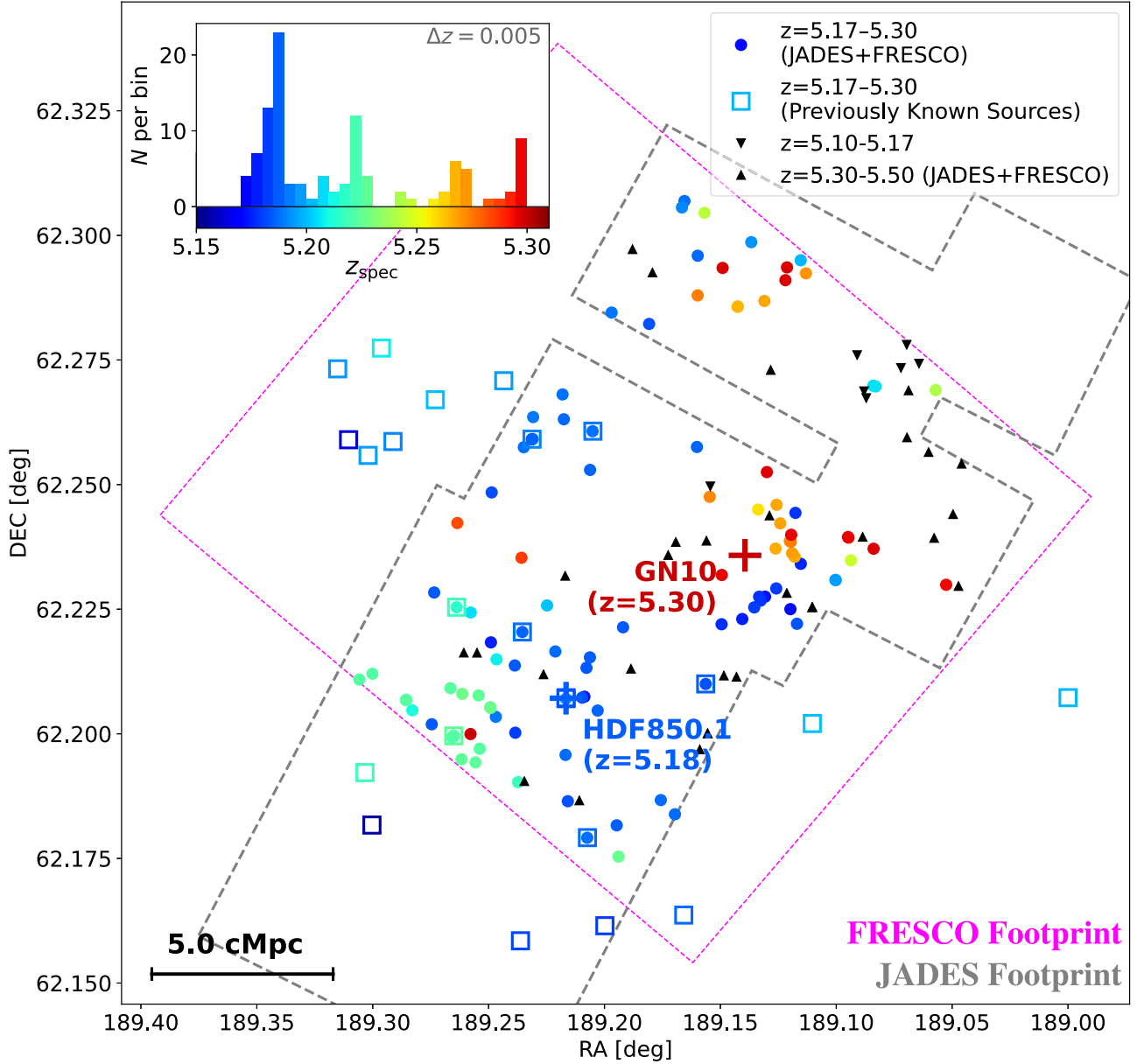
Figure 9. On-sky distribution of 146 Hα-emitting galaxies at $z = 5.1$–5.5 selected with JADES photometry and confirmed with FRESCO. Galaxies at $z = 5.17$–5.30 are shown in filled circles color-coded by their redshifts, and the redshift distribution (bin size $\Delta z = 0.005$) is shown as the inset panel in the upper left corner. Galaxies at $z = 5.10$–5.17, and $z = 5.30$–5.50 are denoted by downward and upward black triangles, respectively. Spectroscopically confirmed galaxies in the $z \sim 5.2$ overdensity before the JWST (Walter et al. 2012; Calvi et al. 2021) are shown in open squares, color-coded by their redshifts. HDF850.1 and another luminous SMG, GN10 at $z = 5.30$ (Wang et al. 2004; Pope et al. 2005; Riechers et al. 2020), are shown in blue and red plus signs, respectively. The footprint of JADES and FRESCO are shown in dashed gray and magenta polygons, respectively. A scale bar of 5 comoving Mpc at $z = 5.2$ is shown in the lower left corner for comparison.

Appendix. We found five point-like sources in our spectroscopic sample with broad Hα line emission with FWHM $\sim 2000 \, \mathrm{km \, s^{-1}}$, which could be interpreted as active galaxy nuclei (AGNs) with bolometric luminosities of $L_{\mathrm{bol}} \simeq 10^{45}$–$10^{46} \, \mathrm{erg \, s^{-1}}$. These sources will be presented and discussed in a companion paper (E. Egami et al. 2023, in preparation; see also Matthee et al. 2023).

In the redshift histogram, we identify four peaks at $z = 5.185$, 5.222, 5.268, and 5.296. In the 1D redshift space with bin size of $\Delta z = 0.005$, these peaks are 36 ± 5, 17 ± 3, 8 ± 2, and 12 ± 2 times more overdense compared with random field galaxies at $z = 5.10$–5.17 and 5.30–5.50. We also evaluate the galaxy overdensity $\delta_g = n/\bar{n} - 1$ in the 3D space, where n is the volume density of galaxies in an

overdense region, and $\bar{n}$ is the volume density of field galaxies. We derive $\bar{n} = 10^{-2.8 \pm 0.1} \, \mathrm{cMpc^{-3}}$ from 37 field galaxies at $z = 5.10$–5.17 and 5.30–5.50. Note that the actual volume density of Hα emitters at this redshift (see Sun et al. 2023) should be higher than $\bar{n}$ because of completeness corrections. Galaxies in our sample share a similar selection function across $z = 5.1$–5.5 on account of the Lyα dropout in the HST F775W band and Hα excess in the NIRCam F410M band, and thus, the use of $\bar{n}$ is fair for galaxies in and out of the overdense environment. Assuming a search radius of $5.5 \, \mathrm{cMpc}$ ($\Delta V \sim 700 \, \mathrm{cMpc^3}$) in which we expect one random field Hα emitter, the galaxy overdensities at the aforementioned four redshift peaks are found to be $\delta_g = 25$, 20, 9, and 7, respectively. The significances of these overdensities assuming
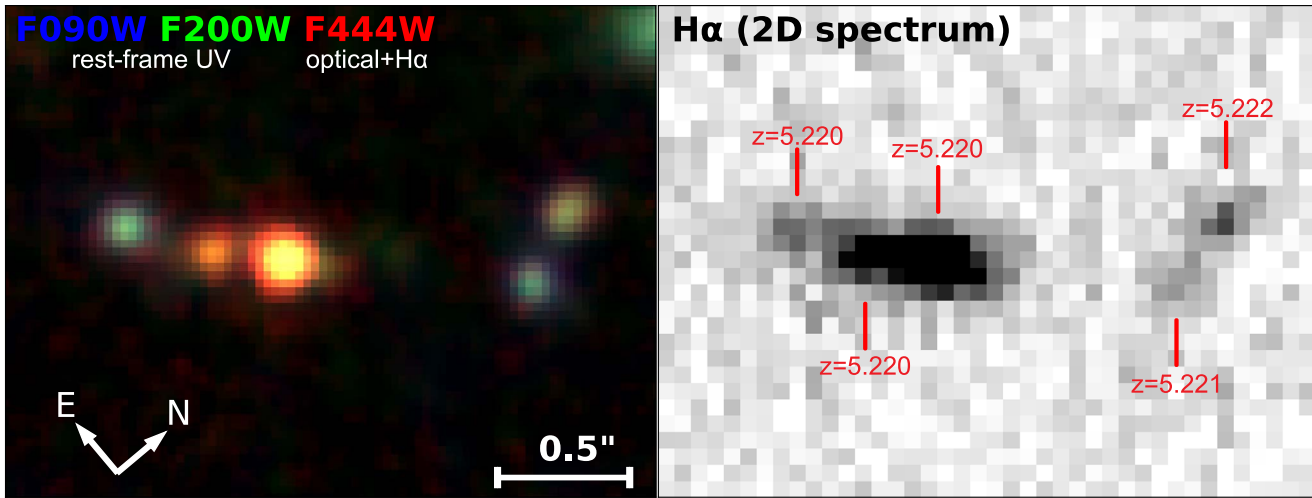
Figure 10. NIRCam F444W-F200W-F090W RGB image (left) and F444W grism spectrum (right) of five Hα-emitting galaxies at $z = 5.220$–5.222, obtained through the JADES and FRESCO surveys, respectively. The NIRCam image is rotated to align with the dispersion direction. The brightest galaxy in the center (F444W = 25.3 AB mag) is at R.A. = 12:37:03.699, decl. = +62°11′57″.7. Hα redshifts of the five galaxies are noted in the right panel, and the two galaxies on the right (northwest) were spectroscopically confirmed previously at $z_{\mathrm{Ly}\alpha} = 5.224$ (Calvi et al. 2021).

Poisson statistics are 10.9σ, 9.0σ, 5.2σ, and 4.3σ, respectively. No other peak is found to lie above a significance of 3.5σ.

Figure 10 shows the core region of the galaxy overdensity corresponding to the second redshift peak at $z = 5.22$. Five galaxies are spectroscopically confirmed at $z = 5.220$–5.222 within a separation of $2''$ ($\sim$12 proper kpc, hereafter pkpc), making it the most overdense region of $z > 5$ galaxies in the joint footprint of JADES and FRESCO in the GOODS-N field. Similar compact assemblies of $z \gtrsim 5$ galaxies have been reported in recent JWST/NIRCam studies (Helton et al. 2023; Jin et al. 2023), which are suggested as the progenitors of massive galaxies (stellar mass $M_{\mathrm{star}} \gtrsim 10^{11}\ M_\odot$) seen at lower redshifts. The two galaxies to the northwest of the bright central galaxy are blended in ground-based images obtained with the SHARDS survey (SHARDS20013448; Pérez-González et al. 2013; Arrabal Haro et al. 2018), which were later spectroscopically confirmed at $z = 5.224$ through the detection of Lyα emission (Calvi et al. 2021). The velocity offset between Lyα and Hα emission is $120 \pm 50\ \mathrm{km\,s}^{-1}$.

A total of eight galaxies in our sample have been reported as part of the $z \sim 5.2$ overdensity through ground-based spectroscopy (Walter et al. 2012; Calvi et al. 2021). The remaining 14 galaxies that are known as part of the overdensity are outside of our JADES and FRESCO joint footprint, suggesting that a significant fraction of overdensity member galaxies are not included in our sample (see also recent study by Herard-Demanche et al. 2023). Indeed, through the JADES photometric redshift analyses, we have identified galaxies outside of the FRESCO footprint that are likely associated with the HDF850.1 overdensity. These sources will be presented in a forthcoming clustering analysis paper from the JADES collaboration (J. Helton et al. 2023, in preparation).

5.2. Clustering Analysis

We adopt a Friends-of-Friends (FoF) algorithm to identify groups among 109 galaxies at $z = 5.17$–5.30 in 3D space. Galaxy groups are selected iteratively, consisting of galaxies that have projected separations and LOS velocity offsets below the adopted linking parameters of $d_{\mathrm{link}} = 500$ pkpc, and

$\Delta v = 500\ \mathrm{km\,s}^{-1}$, respectively. These parameters are identical to those adopted in Calvi et al. (2021, same overdense environment), Helton et al. (2023, same selection technique), which are motivated by the typical virial radius and velocity dispersion of galaxy groups.

We identify four groups of galaxies within the overdense environment with numbers of confirmed members at $N \geqslant 7$. Figure 11 presents the group identification of galaxies in 3D space. The largest group found over the full volume of $16 \times 18 \times 64\ \mathrm{cMpc}^3$ contains 55 member galaxies at $z = 5.17$–5.23, including HDF850.1 (group-1). In the R.A., decl., and redshift direction, the coordinates of galaxies are computed as their offsets to HDF850.1 in comoving distance, but we also warn that the redshift-space distortion effect (e.g., Kaiser 1987) could complicate the actual LOS distance by $\Delta d_{\mathrm{LOS}} \sim 10$ cMpc with $\Delta v = 1000\ \mathrm{km\,s}^{-1}$ ($\Delta z = 0.02$ at $z = 5.2$), which is commonly seen in low-redshift clusters (Struble & Rood 1999). Also as argued in Section 5.1, a significant number of member galaxies at this redshift could be missed because they do not fall in the joint footprint of JADES and FRESCO. The noticeable gap in our survey area (around R.A. = 189°.16, decl. = +62°.26; Figure 9) caused by the gap between the two NIRCam modules prevents us from selecting potential overdensity members in this region. If galaxies at $z = 5.26$–5.30 exist in this region, they can potentially connect the galaxies currently classified as field sources to the north of groups-3 and -4, or even bridge the gap of groups-3 and -4 in redshift space. Indeed, three substructures presented by Calvi et al. (2021) in the same overdense region are now connected in group-1 through our clustering analysis.

The phase-space diagram of groups-1 and -2 at $z = 5.16$–5.23 is shown as Figure 12. In local or low-redshift virialized galaxy clusters, the scattering of peculiar velocity of cluster members decreases at a larger projected distance from the cluster center, which is a natural result with a Navarro–Frenk–White–like dark matter halo profile (Navarro et al. 1996). This is not seen in the phase-space diagram of HDF850.1 overdensity, suggesting that the protocluster has not yet evolved into a dynamically relaxed system.
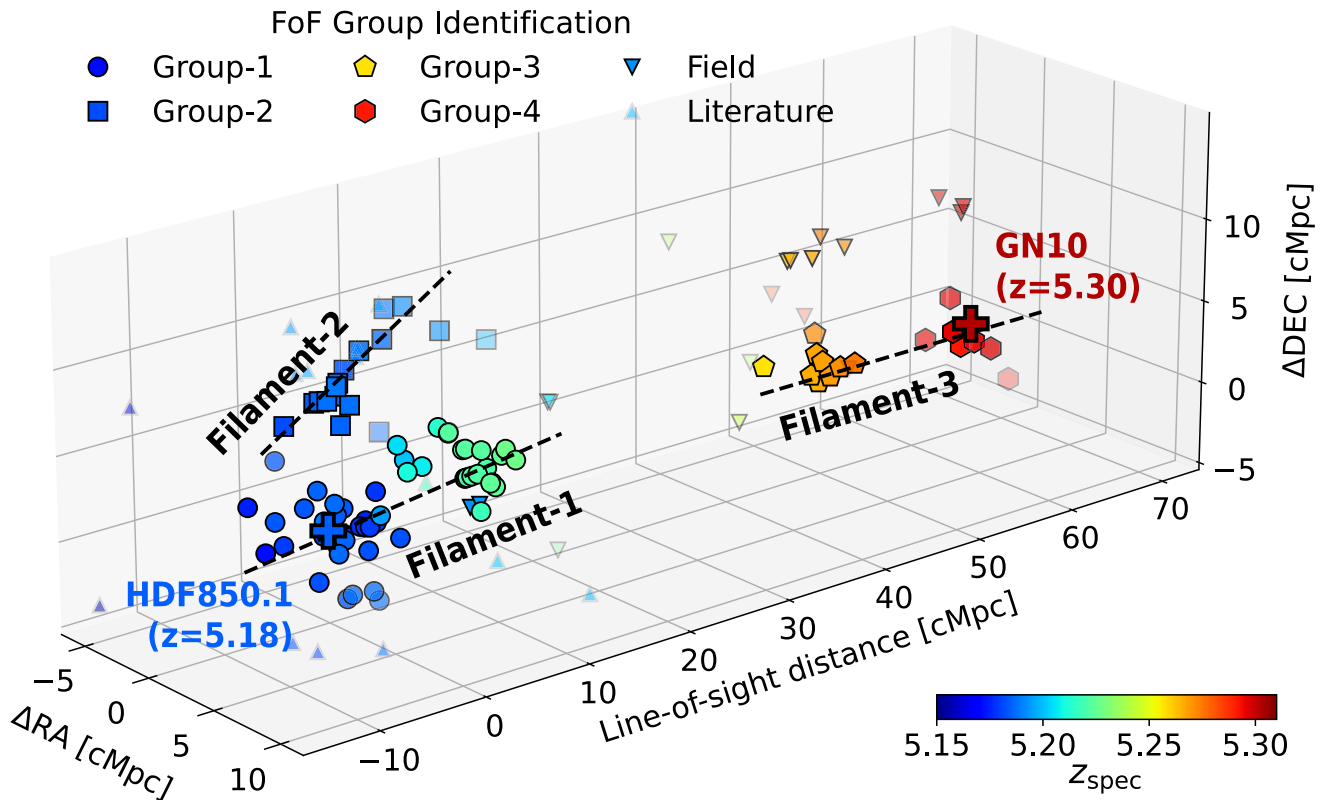
Figure 11. 3D large-scale structure of the overdense environment in the GOODS-N field at $z = 5.17$–5.30. Coordinates of galaxies are with respect to that of HDF850.1 in units of comoving Mpc. All galaxies are color-coded by their redshifts, and galaxies in less dense regions (suggested by Gaussian kernel density estimation) are shown as transparent symbols. Spectroscopically confirmed galaxies in Walter et al. (2012), Calvi et al. (2021) that are not part of our sample are denoted as upward triangles. Through our clustering analysis, we identify four galaxy groups in the overdensities, potentially consisting of three filamentary structures over a volume of $16 \times 18 \times 64$ cMpc^3. The massive SMGs HDF850.1 and GN10 (shown as colored plus signs) reside in our proposed Filament-1 and -3, respectively.

5.3. Filamentary Structure

Cosmological simulations have suggested that $\sim$90% of baryonic and dark matter at $z \gtrsim 5$ resides in unvirialized filamentary large-scale structure (e.g., Haider et al. 2016). We find that the distribution of group member galaxies in 3D space can be potentially interpreted by three filamentary structures (Figure 11). Filament-1 (traced by group-1) and Filament-3 (traced by groups-3 and -4) are structures elongated primarily along the LOS direction with lengths of $\sim$30 cMpc. We warn that the peculiar velocities may lead to the identification of filaments along the LOS that are artificially long, although the peculiar velocities seen in each redshift clustering are rather small ($\sigma_V \lesssim 300$ km s^{-1}, corresponding to $\sigma d_{\mathrm{LOS}} \lesssim 3$ cMpc). Filament-3 is only anchored by two groups of galaxies, and they could be two cospatial groups infalling to the same gravitational potential with opposite velocities. Filament-2 (group-2) elongates along both the decl. and redshift direction with a length of $\sim$15 cMpc, with an rms width in the transverse direction of $\sim$1.6 cMpc.

It is interesting that the redshift differences between galaxies in Filament-2 and HDF850.1 decline with smaller projected distances to HDF850.1 (Figure 12), and therefore, the two filaments could be physically related with the region close to HDF850.1 as the potential node of the cosmic web. Given our current survey volume, the redshift gap between Filament-1 and -3 is real because our selection function (based on photometric redshifts and Hα line detections) does not discriminate galaxies at

this specific redshift. However, there is a chance that the two filaments are linked with faint galaxies whose Hα line luminosities are below our detection limit or through galaxies outside of our survey area. It is worth mentioning again that 14 out of 22 galaxies spectroscopically confirmed previously in the $z \sim 5.2$ protocluster (Walter et al. 2012; Calvi et al. 2021) are outside of the JADES and FRESCO joint footprint, and we do expect more complicated substructures of the overdensity to be uncovered with NIRCam grism or NIRSpec microshutter assembly observations (e.g., GO-2674; PI: Arrabal Haro), which may or may not support our current filamentary interpretation of the large-scale structure.

As one of the most massive galaxies at $z > 5$ in the GOODS-N field, HDF850.1 resides in the core region of Filament-1 with 11 galaxies in its 500 pkpc proximity. Although we do not directly detect the cold gas in this overdensity, the existence of filamentary large-scale structures in the protocluster environment, if real, suggests efficient gas inflow from the intergalactic medium through the cosmic web (e.g., Narayanan et al. 2015), which could be responsible for triggering the intense starburst and rapid assembly of the massive stellar component in HDF850.1 despite a short molecular gas depletion timescale (e.g., Casey 2016). Similarly, another HST-dark SMG, GN10 ($z = 5.303$, see NIRCam images and grism spectrum in Appendix; Wang et al. 2004; Pope et al. 2005; Riechers et al. 2020), resides at the high-redshift end of Filament-3. Calvi et al. (2023) discovered that GN10 also traces an overdense environment through photometric redshift analysis
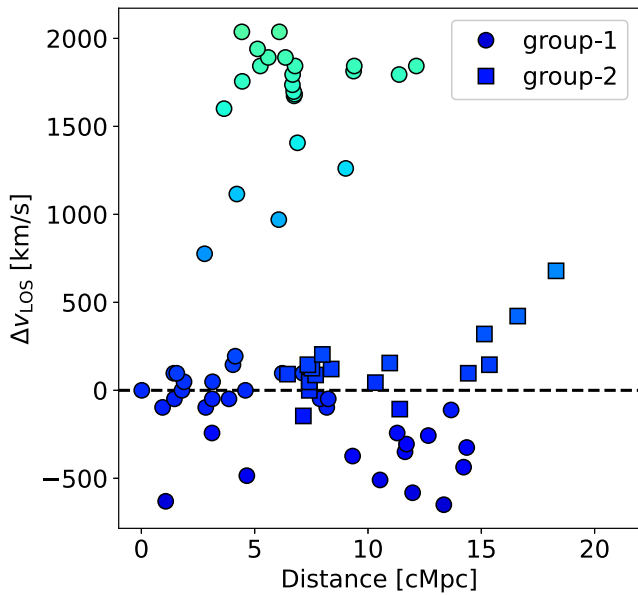
Figure 12. Phase-space diagram of galaxies in groups-1 (circles) and -2 (squares) classified with FoF algorithm (Section 5.2). The projected distances and line-of-sight velocity offsets are with respect to HDF850.1. Galaxies are color-coded by redshifts (same as that in Figures 9 and 11).
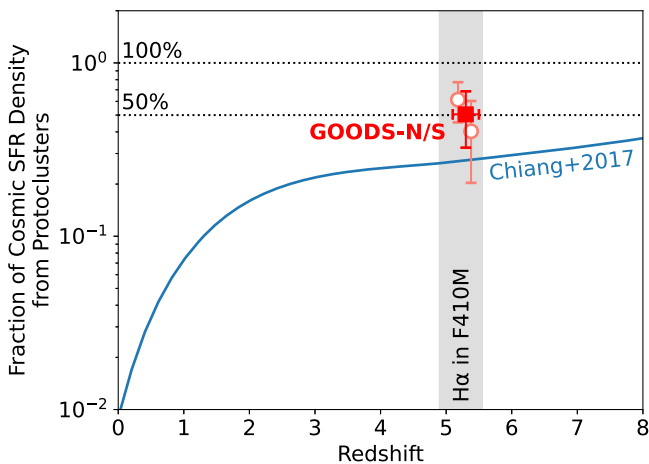

Figure 13. Fraction of cosmic SFR density from protoclusters as a function of redshift. The constraints from Hα emitters at $z = 5.1$–5.5 in both the GOODS-N (this work) and GOODS-S (Helton et al. 2023) fields are shown as the open circles (for each field) or the filled red square (combined). Model prediction from Chiang et al. (2017) is shown as the solid blue line.

by applying the well-established poisson probability method (Castignani et al. 2014, 2019), and our study provides the crucial spectroscopic confirmation with NIRCam grism spectroscopy (see also Herard-Demanche et al. 2023).

5.4. The Ubiquity of Galaxy Overdensities at $z \sim 5$

Helton et al. (2023) reported the discovery of a galaxy protocluster in the GOODS-S field with 43 confirmed members at $z = 5.4$ using the same selection method that we have used (NIRCam photometric redshifts and grism redshift confirmation with Hα). These galaxies were selected in a 41 arcmin^2 joint survey area with JADES and FRESCO, and 53 field galaxies that are not part of the overdensity were confirmed at $z = 5.2$–5.5.

It is certainly an interesting fact that both GOODS fields host galaxy overdensities at comparable redshifts. At these redshifts, Hα lines are within the bandwidth of the F410M filter. Note that JADES did not preferentially target both fields for overdensity mapping. Both of the overdensities can be detected and characterized at high fidelity with a comoving survey volume of $\sim 4 \times 10^4$ cMpc^{-3} in each field, and both could evolve into Coma-like clusters in the present Universe (Calvi et al. 2021; Helton et al. 2023). In fact, the expected dark matter halo mass of HDF850.1 itself based on its stellar mass is already $M_{\rm halo} = 10^{12.5}$–$10^{13}\,M_{\odot}$ using the empirical $M_{\rm star}$–$M_{\rm halo}$ relation, at $z = 5$ from Behroozi et al. (2019), which is similar to or greater than the halo mass of the progenitor of Coma cluster at this redshift based on simulations (Chiang et al. 2013).

These findings may suggest that massive galaxy overdensities in the high-redshift Universe are fairly common. In fact, similar overdensities at $z \simeq 5$–6 have also been reported along the sight line of $z > 6$ quasars in EIGER (Kashino et al. 2023) and ASPIRE (Wang et al. 2023) surveys through JWST/ NIRCam slitless spectroscopy. If we assume that the Hα luminosity functions in and out of an overdense environment share the same shape but with different normalizations, we can roughly estimate the fraction of instantaneous cosmic SFR density hosted in protocluster environments through the number fraction of Hα emitters. With the JADES and FRESCO joint survey in the GOODS-S/N fields, we estimate that $\sim 50\%$ of cosmic SFR densities are hosted in protoclusters at $z \sim 5.2$, which is slightly higher than the fraction of $\sim 30\%$ as suggested by simulations (Chiang et al. 2017; see Figure 13).

The discrepancy between derived and predicted fraction of cosmic SFR densities from protoclusters could arise from the cosmic variance ($\sigma \sim 20\%$; Trenti & Stiavelli 2008), the difference in the shapes of Hα luminosity functions in and out of protoclusters, and also the fraction of obscured cosmic SFR densities in two distinct environments. In fact, if we sum the Hα luminosities of galaxies in and out of overdensities, then $\sim 60\%$ of Hα luminosity density above our detection limit ($L_{\rm H\alpha} \gtrsim 6 \times 10^{41}\,{\rm erg\,s^{-1}}$, 5σ) is from protocluster member galaxies. A large cosmic variance is indeed observed, as the protocluster in the GOODS-N field is more overdense than the one in the GOODS-S field (Helton et al. 2023) by a factor of ~ 2.

6. Summary

In this paper, we have studied the stellar component and overdense environment of HDF850.1 at $z = 5.18$, the brightest SMG in the Hubble Deep Field. By combining JWST/ NIRCam 0.8–5.0 μm imaging observations obtained with JADES and 3.9–5.0 μm WFSS observation obtained with FRESCO, we detect and resolve the rest-frame optical stellar component of HDF850.1 for the first time since its discovery (Hughes et al. 1998). We also detect the Hα line emission from HDF850.1 through grism spectroscopy. In addition, we identify 109 galaxies in the redshift range of $z = 5.17$–5.30, where only eight galaxies were spectroscopically confirmed previously. Our main conclusions are summarized as follows:

1. HDF850.1 is split into two components in NIRCam images because of heavy dust attenuation in the center. Through pixelated SED modeling, we reconstruct the map of Hα emission, dust attenuation (A_V), and the stellar

mass distribution. The northern component is higher in A_V with lower Hα surface brightness, and the southern component is lower in A_V and leaks rest-frame UV and Hα photons. The location of the high-A_V region matches well with that of dust emission as observed with PdBI (Neri et al. 2014).

2. After correcting for a lensing magnification of $\bar{\mu} = 2.5$, we derive the stellar mass($\log(M_{\rm star}/M_\odot) = 10.8 \pm 0.1$), SFR ($\log[{\rm SFR}/(M_\odot\,{\rm yr}^{-1})] = 2.8 \pm 0.2$ based on mid-to-far-IR SED modeling), and dust attenuation ($A_V = 4.6 \pm 0.7$) for HDF850.1. As one of the most massive galaxies at $z > 5$, most of the star formation of HDF850.1 is dust-obscured. This places HDF850.1 at the massive end of the star-forming main sequence at $z \sim 5$.

3. After correcting for dust attenuation, we find that the morphology of HDF850.1 can be well described by a single galaxy. In the image plane (lensing-uncorrected), we measure a half-mass–radius of $0\farcs27 \pm 0\farcs02$ from the 1D profile, which is smaller than the half-light radius in rest-frame V band ($0\farcs49 \pm 0\farcs02$). This is because the high dust attenuation in the galaxy center flattens out the light profile.

4. The Hα emission of HDF850.1 is detected spectroscopically with NIRCam WFSS. The Hα redshift is consistent with that of [C II] measured with PdBI (Walter et al. 2012; Neri et al. 2014), and the morphology of Hα emission in the 2D grism spectrum is also consistent with that derived from pixelated fitting of imaging data. We also resolve the kinematics of HDF850.1 through the Hα line, and we find a velocity offset of 330 ± 70 km s^{-1} from the Hα centroid of the southern component to the galaxy center.

5. Through morphological and kinematic information, we conclude that HDF850.1 is not necessarily a major-merger system in the final coalescence phase. However, our observations cannot rule out the potential existence of a minor merger, or even a major merger in the past SFH.

6. Despite the high dust attenuation and HST-dark nature (>28 AB mag below 1.6 μm), the dust attenuation of HDF850.1 is inhomogeneous, placing it $\sim$100 times above the empirical IRX–$\beta_{\rm UV}$ relation at its UV continuum slope (-0.8 ± 0.2). HDF850.1 is compact in both stellar mass and dust continuum emission (half-mass and/or light radius of 1.0 ± 0.1 kpc in the source plane), which is likely the cause of the high dust attenuation seen for the system.

7. Leveraging off JADES high-accuracy photometric redshifts, we spectroscopically confirm 146 galaxies in the joint footprint of JADES and FRESCO at $z = 5.1$–5.5 with $\geqslant 5\sigma$ detections of Hα lines. 109 of them are in the narrower redshift range of $z = 5.17$–5.30, in which four peaks of redshift clustering are detected at $z = 5.185$, 5.222, 5.268, and 5.296 with significance greater than 4σ. Among this sample, only eight sources were spectroscopically confirmed previously as members of the $z = 5.2$ protocluster (Walter et al. 2012; Calvi et al. 2021). Fourteen galaxies that were confirmed as members of this protocluster are outside of our survey area, suggesting that a significant fraction of member galaxies and substructures are missed with this study.

8. Through an FoF clustering analysis, we identify four $N \geqslant 7$ groups of galaxies at $z = 5.17$–5.30. The grouped galaxies in 3D space can be interpreted in terms of three filamentary structures with lengths of 15–30 cMpc.

HDF850.1 resides in one filament, and it potentially serves as a node of the cosmic web by connecting to another filament. Another SMG (GN10) at $z = 5.30$ is associated with the third proposed filament. If these filamentary structures are real, the efficient cold gas inflow through the cosmic web can be responsible for the vigorous starburst and rapid mass assembly of luminous SMGs at this epoch.

9. Both the GOODS-N/S fields are now confirmed to contain galaxy protoclusters at $z = 5.2$–5.4 (Calvi et al. 2021; Helton et al. 2023; and this work). This may suggest that Coma-progenitor-like galaxy overdensities in the high-redshift Universe are fairly common. From our observed fraction of Hα emitters associated with galaxy protoclusters at $z = 5.1$–5.5, we estimate that $50\% \pm 20\%$ of cosmic SFR density occurs in the protocluster environment at this epoch. This may be slightly higher than previous simulation predictions ($\sim$30%; Chiang et al. 2017), but our estimate is subject to a variety of uncertainties, e.g., cosmic variance and the difference in Hα luminosity function shapes in and out of overdense environments.

Appendix
NIRCam Cutout Images and Grism Spectra of Confirmed Galaxies at $z = 5.1$–5.5

Figure A1 shows the NIRCam cutout images and extracted 2D and 1D grism spectra for 140 galaxies at $z = 5.1$–5.5 that

we spectroscopically confirmed with $\geqslant 5\sigma$ detection of Hα line emission. The properties of galaxies in this sample are presented in Table 2. We note that the spectrum of HDF850.1 is not shown in this figure because it is presented in Figure 6. The cutout images and spectra of five AGN candidates identified through broad Hα emission lines are also not shown in the table. They will be presented and studied in detail with a companion paper (E. Egami et al. 2023, in preparation; also Matthee et al. 2023).

GN10 ($z = 5.303$; R.A. = 12°36′33.398, decl. = +62°14′08″.4) is another luminous SMG that is within the overdense environment. This source is not included in our photometric-redshift parent sample because of heavy dust obscuration, which leads to a large uncertainty of $z_{\rm phot}$. Figure A2 shows the NIRCam images and grism spectrum of GN10. GN10 is also an HST-dark SMG and only detected at above 2 μm. Multiple components could be identified from the image, suggesting a hint of merger nature. In the NIRCam grism spectrum, we detect the Hα ($(9.5 \pm 0.9) \times 10^{-18}$ erg s^{-1} cm^{-2}) and [N II] $\lambda6583$ ($(4.9 \pm 0.8) \times 10^{-18}$ erg s^{-1} cm^{-2}) line emission at $z = 5.303$, the same redshift reported previously through CO lines (Riechers et al. 2020).

For completeness, we also show the full NIRCam 1D grism spectra (3.90–4.85 μm) of HDF850.1 and GN10 in Figure A3. We note that the spectrum of GN10 is contaminated by a bright galaxy at $z = 1.381$, whose [Fe II] $\lambda1.646\,\mu$m and Paschen α lines are visible in the 1D spectrum. These interloping emission lines are marked for clarity.
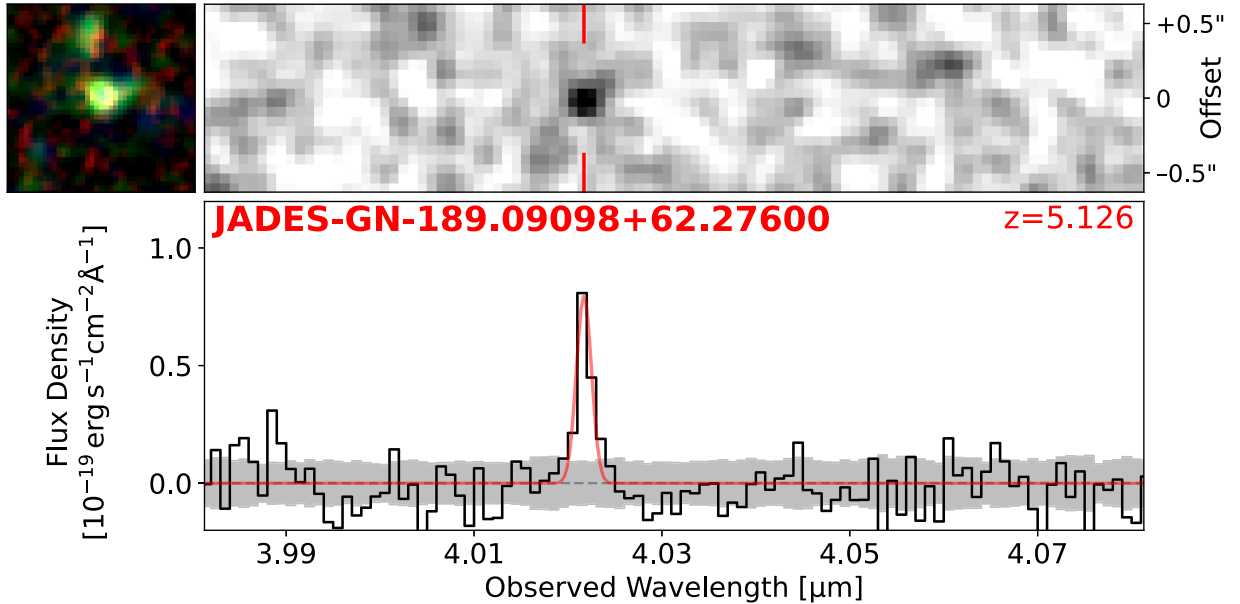
Figure A1. NIRCam images, 2D and 1D grism spectra of JADES-GN-189.09098+62.27600 at $z = 5.126$. The upper left panel shows the $1''\!.2 \times 1''\!.2$ F444W–F277W–F150W RGB thumbnail. Images are rotated to align with the dispersion direction. The upper right panel shows the continuum-subtracted 2D spectrum around the Hα emission-line detection, indicated by the solid red line. The lower right panel shows the optimally extracted 1D spectrum with the best-fit Gaussian profile indicated by the solid red line. The name and confirmed spectroscopic redshift are given in the lower right panel for each galaxy.

(The complete figure set of 140 images is available.)

Table 2
Summary of Spectroscopically Confirmed Hα-emitting Galaxies at $z = 5.1$–5.5

Index	Name	R.A. (deg)	Decl. (deg)	z_{spec}	M_{UV} (mag)	F444W (mag)	Hα Line Flux (10^{-18} erg s^{-1} cm^{-2})?	Group
1	JADES-GN-189.06961+62.27808	189.06961	+62.27808	5.115	-18.71 ± 0.08	27.80	2.06 ± 0.27	F
2	JADES-GN-189.09098+62.27600	189.09098	+62.27600	5.126	-18.38 ± 0.12	27.71	1.61 ± 0.19	F
3	JADES-GN-189.08706+62.26738	189.08706	+62.26738	5.131	-18.72 ± 0.06	27.14	5.64 ± 0.47	F
4	JADES-GN-189.15434+62.24967	189.15434	+62.24967	5.141	-19.71 ± 0.03	27.25	3.07 ± 0.48	F
5	JADES-GN-189.08801+62.26874	189.08801	+62.26874	5.141	-20.39 ± 0.03	25.92	4.97 ± 0.56	F
6	JADES-GN-189.06429+62.27429	189.06429	+62.27429	5.145	-19.45 ± 0.03	26.44	4.82 ± 0.32	F
7	JADES-GN-189.11978+62.22501	189.11978	+62.22501	5.172	-19.30 ± 0.11	27.25	2.73 ± 0.42	1
8	JADES-GN-189.20867+62.20743	189.20867	+62.20743	5.172	-20.30 ± 0.03	25.52	12.34 ± 1.07	1
9	JADES-GN-189.13071+62.22752	189.13071	+62.22752	5.173	-18.92 ± 0.15	27.50	1.96 ± 0.26	1
10	JADES-GN-189.14055+62.22303	189.14055	+62.22303	5.175	-19.12 ± 0.06	27.18	3.00 ± 0.42	1
11	JADES-GN-189.24900+62.21834	189.24900	+62.21834	5.175	-18.94 ± 0.03	27.24	2.93 ± 0.43	1
12	JADES-GN-189.11531+62.23411	189.11531	+62.23411	5.176	-19.24 ± 0.09	27.02	4.36 ± 0.33	1
13	JADES-GN-189.14948+62.22198	189.14948	+62.22198	5.177	-20.11 ± 0.03	26.32	3.07 ± 0.49	1
14	JADES-GN-189.13328+62.22751	189.13328	+62.22751	5.178	-20.17 ± 0.03	25.03	17.08 ± 0.73	1
15	JADES-GN-189.11761+62.24433	189.11761	+62.24433	5.178	-19.52 ± 0.10	26.84	3.00 ± 0.36	1
16	JADES-GN-189.13261+62.22674	189.13261	+62.22674	5.179	-19.66 ± 0.03	26.32	5.66 ± 0.36	1
17	JADES-GN-189.12590+62.22916	189.12590	+62.22916	5.180	-20.27 ± 0.03	25.54	9.21 ± 0.47	1
18	JADES-GN-189.13539+62.22536	189.13539	+62.22536	5.180	-20.64 ± 0.03	25.74	10.63 ± 0.49	1
19	JADES-GN-189.23848+62.20022	189.23848	+62.20022	5.180	-18.92 ± 0.04	26.48	3.25 ± 0.47	1
20	JADES-GN-189.24868+62.24843	189.24868	+62.24843	5.182	-19.57 ± 0.03	25.21	13.00 ± 0.71	2
21	JADES-GN-189.11695+62.22208	189.11695	+62.22208	5.183	-19.73 ± 0.03	26.38	5.00 ± 0.39	1
22	JADES-GN-189.18074+62.28224	189.18074	+62.28224	5.183	-20.02 ± 0.06	25.49	9.84 ± 0.45	2
23	JADES-GN-189.15632+62.21000	189.15632	+62.21000	5.183	-19.89 ± 0.03	25.84	5.57 ± 0.43	1
24	JADES-GN-189.21582+62.18648	189.21582	+62.18648	5.183	-19.55 ± 0.03	25.46	14.99 ± 0.40	1
25	JADES-GN-189.20968+62.20726	189.20968	+62.20726	5.183	-19.75 ± 0.03	26.65	4.77 ± 0.52	1
26	JADES-GN-189.27453+62.20191	189.27453	+62.20191	5.184	-18.50 ± 0.06	27.97	1.56 ± 0.25	1
27	JADES-GN-189.20777+62.21324	189.20777	+62.21324	5.184	-19.99 ± 0.03	25.38	10.43 ± 0.82	1
28	JADES-GN-189.23869+62.21371	189.23869	+62.21371	5.184	-20.33 ± 0.03	26.14	3.01 ± 0.51	1
29	JADES-GN-189.19199+62.22137	189.19199	+62.22137	5.184	-18.71 ± 0.05	27.16	3.11 ± 0.41	1
30	JADES-GN-189.27348+62.22835	189.27348	+62.22835	5.184	-20.01 ± 0.03	26.13	3.72 ± 0.62	1
31	JADES-GN-189.20629+62.21533	189.20629	+62.21533	5.185	-19.32 ± 0.03	26.22	5.37 ± 0.37	1
32	JADES-GN-189.19472+62.18163	189.19472	+62.18163	5.185	-19.08 ± 0.03	27.40	3.13 ± 0.41	1
33	JADES-GN-189.23137+62.25908	189.23137	+62.25908	5.185	-20.09 ± 0.03	25.82	23.78 ± 0.59	2
34	JADES-GN-189.16011+62.25755	189.16011	+62.25755	5.186	-19.20 ± 0.05	26.08	5.49 ± 0.61	2
35	JADES-GN-189.23545+62.22043	189.23545	+62.22043	5.186	-19.66 ± 0.03	26.65	4.52 ± 0.45	1
36	JADES-GN-189.23124+62.25913	189.23124	+62.25913	5.186	-20.24 ± 0.03	25.89	24.48 ± 0.59	2
37	JADES-GN-189.23103+62.25912	189.23103	+62.25912	5.186	-19.67 ± 0.03	26.47	15.82 ± 0.59	2
38	JADES-GN-189.20293+62.20467	189.20293	+62.20467	5.186	-19.73 ± 0.03	24.56	40.83 ± 1.19	1
39	JADES-GN-189.20621+62.25295	189.20621	+62.25295	5.186	-17.63 ± 0.21	26.65	1.20 ± 0.39	2
40	JADES-GN-189.21754+62.26311	189.21754	+62.26311	5.187	-19.27 ± 0.10	27.38	2.01 ± 0.36	2
41	JADES-GN-189.21680+62.19577	189.21680	+62.19577	5.187	-19.40 ± 0.03	26.09	8.14 ± 0.77	1
42	JADES-GN-189.22121+62.21652	189.22121	+62.21652	5.187	-19.57 ± 0.03	26.32	4.42 ± 0.66	1
43	JADES-GN-189.17570+62.18671	189.17570	+62.18671	5.187	-19.95 ± 0.03	25.42	7.37 ± 0.71	1
44	JADES-GN-189.16961+62.18386	189.16961	+62.18386	5.187	-19.40 ± 0.04	26.75	5.13 ± 0.52	1
45	JADES-GN-189.21809+62.26809	189.21809	+62.26809	5.188	-20.65 ± 0.03	24.96	5.18 ± 0.63	2
46	JADES-GN-189.20512+62.26072	189.20512	+62.26072	5.188	-21.09 ± 0.03	25.45	16.10 ± 0.44	2
47	JADES-GN-189.20744+62.17914	189.20744	+62.17914	5.188	-19.57 ± 0.04	26.42	4.41 ± 0.33	1
48	JADES-GN-189.23482+62.25750	189.23482	+62.25750	5.188	-20.21 ± 0.03	25.51	10.84 ± 0.38	2
49	JADES-GN-189.16549+62.30689	189.16549	+62.30689	5.188	-19.96 ± 0.03	26.21	3.02 ± 0.30	2
50	JADES-GN-189.19692+62.28451	189.19692	+62.28451	5.188	-20.21 ± 0.03	26.00	3.52 ± 0.27	2
51	JADES-GN-189.24689+62.20341	189.24689	+62.20341	5.189	-19.02 ± 0.04	25.98	5.32 ± 0.77	1
52	JADES-GN-189.23078+62.26355	189.23078	+62.26355	5.189	-19.87 ± 0.03	26.71	5.21 ± 0.35	2
53	JADES-GN-189.16658+62.30560	189.16658	+62.30560	5.192	-20.20 ± 0.04	24.48	11.78 ± 0.56	2
54	JADES-GN-189.10025+62.23082	189.10025	+62.23082	5.193	-19.53 ± 0.08	26.73	4.24 ± 0.69	F
55	JADES-GN-189.13667+62.29864	189.13667	+62.29864	5.194	-18.67 ± 0.09	27.72	1.19 ± 0.18	2
56	JADES-GN-189.10034+62.23089	189.10034	+62.23089	5.195	-19.21 ± 0.05	26.61	5.75 ± 0.62	F
57	JADES-GN-189.11534+62.29500	189.11534	+62.29500	5.199	-19.16 ± 0.12	26.96	3.30 ± 0.31	2
58	JADES-GN-189.22478+62.22575	189.22478	+62.22575	5.201	-18.31 ± 0.08	26.77	1.74 ± 0.21	1
59	JADES-GN-189.25771+62.22433	189.25771	+62.22433	5.205	-18.81 ± 0.04	26.77	2.24 ± 0.41	1
60	JADES-GN-189.08401+62.26984	189.08401	+62.26984	5.205	-18.42 ± 0.19	27.76	1.92 ± 0.28	F
61	JADES-GN-189.08302+62.26969	189.08302	+62.26969	5.206	-18.98 ± 0.03	27.20	2.57 ± 0.31	F
62	JADES-GN-189.24659+62.21494	189.24659	+62.21494	5.208	-19.87 ± 0.03	25.25	15.67 ± 0.82	1
63	JADES-GN-189.28294+62.20472	189.28294	+62.20472	5.211	-19.23 ± 0.03	27.33	3.10 ± 0.28	1

Table 2
(Continued)

Index	Name	R.A. (deg)	Decl. (deg)	z_{spec}	M_{UV} (mag)	F444W (mag)	Hα Line Flux (10^{-18} erg s^{-1} cm^{-2})?	Group
64	JADES-GN-189.26381+62.22539	189.26381	+62.22539	5.214	−20.42 ± 0.03	25.49	19.94 ± 0.55	1
65	JADES-GN-189.23731+62.19031	189.23731	+62.19031	5.218	−19.03 ± 0.03	27.25	2.42 ± 0.33	1
66	JADES-GN-189.26554+62.19931	189.26554	+62.19931	5.220	−18.49 ± 0.06	26.58	7.01 ± 1.09	1
67	JADES-GN-189.26569+62.19927	189.26569	+62.19927	5.220	−19.23 ± 0.03	27.04	3.49 ± 1.19	1
68	JADES-GN-189.26541+62.19937	189.26541	+62.19937	5.220	−19.39 ± 0.03	25.27	13.83 ± 1.11	1
69	JADES-GN-189.26502+62.19955	189.26502	+62.19955	5.221	−19.06 ± 0.04	27.49	2.44 ± 0.25	1
70	JADES-GN-189.24928+62.20532	189.24928	+62.20532	5.221	−18.66 ± 0.04	25.66	23.07 ± 5.11	1
71	JADES-GN-189.26510+62.19963	189.26510	+62.19963	5.222	−18.94 ± 0.04	27.13	3.43 ± 0.25	1
72	JADES-GN-189.28549+62.20682	189.28549	+62.20682	5.222	−19.57 ± 0.03	25.91	6.30 ± 0.88	1
73	JADES-GN-189.28570+62.20676	189.28570	+62.20676	5.223	−19.40 ± 0.03	26.44	1.97 ± 1.25	1
74	JADES-GN-189.26643+62.20915	189.26643	+62.20915	5.223	−21.12 ± 0.03	24.77	9.20 ± 0.66	1
75	JADES-GN-189.25382+62.19701	189.25382	+62.19701	5.223	−18.47 ± 0.06	26.83	4.71 ± 0.26	1
76	JADES-GN-189.30578+62.21089	189.30578	+62.21089	5.223	−20.81 ± 0.03	25.81	14.82 ± 0.56	1
77	JADES-GN-189.26168+62.19490	189.26168	+62.19490	5.224	−19.58 ± 0.05	26.40	5.96 ± 0.39	1
78	JADES-GN-189.25565+62.19426	189.25565	+62.19426	5.224	−19.93 ± 0.04	25.75	6.30 ± 0.42	1
79	JADES-GN-189.25428+62.20769	189.25428	+62.20769	5.225	−19.34 ± 0.03	26.51	3.82 ± 0.48	1
80	JADES-GN-189.19396+62.17536	189.19396	+62.17536	5.226	−18.43 ± 0.06	26.55	3.26 ± 0.33	F
81	JADES-GN-189.26137+62.20801	189.26137	+62.20801	5.227	−19.80 ± 0.03	25.71	19.04 ± 0.61	1
82	JADES-GN-189.24913+62.20519	189.24913	+62.20519	5.227	−20.60 ± 0.03	24.89	24.33 ± 0.78	1
83	JADES-GN-189.15686+62.30453	189.15686	+62.30453	5.242	−19.42 ± 0.10	27.18	3.81 ± 0.61	F
84	JADES-GN-189.09366+62.23480	189.09366	+62.23480	5.245	−19.03 ± 0.05	27.16	3.55 ± 0.35	F
85	JADES-GN-189.13369+62.24499	189.13369	+62.24499	5.257	−18.98 ± 0.06	27.00	3.33 ± 0.39	3
86	JADES-GN-189.14244+62.28573	189.14244	+62.28573	5.264	−20.04 ± 0.03	26.14	6.07 ± 1.16	F
87	JADES-GN-189.14260+62.28570	189.14260	+62.28570	5.264	−18.94 ± 0.05	26.71	5.12 ± 0.64	F
88	JADES-GN-189.12617+62.23717	189.12617	+62.23717	5.266	−19.58 ± 0.04	26.83	3.40 ± 0.49	3
89	JADES-GN-189.11794+62.23552	189.11794	+62.23552	5.266	−19.25 ± 0.05	27.25	3.27 ± 0.32	3
90	JADES-GN-189.13100+62.28684	189.13100	+62.28684	5.267	−19.54 ± 0.08	25.48	6.44 ± 0.58	F
91	JADES-GN-189.12574+62.24596	189.12574	+62.24596	5.267	−19.19 ± 0.06	27.16	3.42 ± 0.45	3
92	JADES-GN-189.12415+62.24222	189.12415	+62.24222	5.268	−19.26 ± 0.05	26.73	5.78 ± 0.55	3
93	JADES-GN-189.11906+62.23624	189.11906	+62.23624	5.269	−20.47 ± 0.03	25.99	8.29 ± 0.40	3
94	JADES-GN-189.11309+62.29239	189.11309	+62.29239	5.270	−18.07 ± 0.12	25.24	3.21 ± 0.35	F
95	JADES-GN-189.12004+62.23867	189.12004	+62.23867	5.271	−20.13 ± 0.05	25.94	7.46 ± 0.41	3
96	JADES-GN-189.15458+62.24755	189.15458	+62.24755	5.272	−19.24 ± 0.05	26.33	4.87 ± 0.45	3
97	JADES-GN-189.11960+62.23855	189.11960	+62.23855	5.274	−19.72 ± 0.03	26.59	7.90 ± 0.75	3
98	JADES-GN-189.15980+62.28796	189.15980	+62.28796	5.274	−19.56 ± 0.03	27.07	2.50 ± 0.41	F
99	JADES-GN-189.26349+62.24229	189.26349	+62.24229	5.283	−17.13 ± 0.22	28.02	1.84 ± 0.34	F
100	JADES-GN-189.23581+62.23532	189.23581	+62.23532	5.285	−18.85 ± 0.11	26.88	3.20 ± 0.28	F
101	JADES-GN-189.09470+62.23936	189.09470	+62.23936	5.292	−19.34 ± 0.05	26.13	9.64 ± 0.43	4
102	JADES-GN-189.05259+62.22990	189.05259	+62.22990	5.294	−19.51 ± 0.05	26.18	5.97 ± 0.21	4
103	JADES-GN-189.14939+62.23187	189.14939	+62.23187	5.295	−20.12 ± 0.05	25.41	7.92 ± 0.43	4
104	JADES-GN-189.09492+62.23948	189.09492	+62.23948	5.295	−20.12 ± 0.05	25.71	7.20 ± 0.42	4
105	JADES-GN-189.11943+62.23994	189.11943	+62.23994	5.295	−20.58 ± 0.03	25.01	7.18 ± 0.68	4
106	JADES-GN-189.12993+62.25251	189.12993	+62.25251	5.296	−20.14 ± 0.03	26.44	5.14 ± 0.31	4
107	JADES-GN-189.08389+62.23713	189.08389	+62.23713	5.296	−19.86 ± 0.06	26.51	5.08 ± 0.27	4
108	JADES-GN-189.12192+62.29101	189.12192	+62.29101	5.297	−19.62 ± 0.08	26.31	2.51 ± 0.29	F
109	JADES-GN-189.12124+62.29358	189.12124	+62.29358	5.297	−18.21 ± 0.12	27.32	2.49 ± 0.20	F
110	JADES-GN-189.14903+62.29347	189.14903	+62.29347	5.297	−18.20 ± 0.13	27.55	1.50 ± 0.25	F
111	JADES-GN-189.25780+62.19996	189.25780	+62.19996	5.299	−18.24 ± 0.07	26.96	1.26 ± 0.23	F
112	JADES-GN-189.22631+62.21190	189.22631	+62.21190	5.311	−20.27 ± 0.03	24.98	11.82 ± 0.94	F
113	JADES-GN-189.11031+62.22544	189.11031	+62.22544	5.344	−20.54 ± 0.04	25.47	12.84 ± 1.45	F
114	JADES-GN-189.11044+62.22533	189.11044	+62.22533	5.346	−18.53 ± 0.38	27.06	2.81 ± 0.73	F
115	JADES-GN-189.25501+62.21625	189.25501	+62.21625	5.348	−19.02 ± 0.07	26.89	2.67 ± 0.49	F
116	JADES-GN-189.21696+62.23168	189.21696	+62.23168	5.354	−19.10 ± 0.12	26.68	4.35 ± 0.48	F
117	JADES-GN-189.17252+62.23584	189.17252	+62.23584	5.355	−19.13 ± 0.11	27.55	3.00 ± 0.44	F
118	JADES-GN-189.12134+62.22823	189.12134	+62.22823	5.356	−19.15 ± 0.14	26.66	3.64 ± 0.35	F
119	JADES-GN-189.06016+62.25651	189.06016	+62.25651	5.360	−19.42 ± 0.05	25.98	8.22 ± 0.63	F
120	JADES-GN-189.06947+62.25945	189.06947	+62.25945	5.362	−19.81 ± 0.03	26.10	9.04 ± 0.68	F
121	JADES-GN-189.04592+62.25416	189.04592	+62.25416	5.362	−19.29 ± 0.08	26.39	6.85 ± 0.39	F
122	JADES-GN-189.16922+62.23847	189.16922	+62.23847	5.418	−18.94 ± 0.06	26.05	4.09 ± 0.52	F
123	JADES-GN-189.12883+62.24377	189.12883	+62.24377	5.420	−18.99 ± 0.18	27.40	2.56 ± 0.40	F
124	JADES-GN-189.21086+62.18661	189.21086	+62.18661	5.421	−19.05 ± 0.08	26.86	3.23 ± 0.45	F
125	JADES-GN-189.18858+62.21303	189.18858	+62.21303	5.426	−19.28 ± 0.06	26.94	3.06 ± 0.38	F
126	JADES-GN-189.04727+62.22963	189.04727	+62.22963	5.428	−18.62 ± 0.23	27.75	1.22 ± 0.21	F

Table 2
(Continued)

Index	Name	R.A. (deg)	Decl. (deg)	z_{spec}	M_{UV} (mag)	F444W (mag)	Hα Line Flux (10^{-18} erg s^{-1} cm^{-2})?	Group
127	JADES-GN-189.26070+62.21626	189.26070	+62.21626	5.432	-18.67 ± 0.10	26.97	5.23 ± 0.47	F
128	JADES-GN-189.15602+62.23872	189.15602	+62.23872	5.435	-19.10 ± 0.12	27.76	1.75 ± 0.31	F
129	JADES-GN-189.12828+62.27297	189.12828	+62.27297	5.435	-18.76 ± 0.06	27.77	1.67 ± 0.27	F
130	JADES-GN-189.04962+62.24405	189.04962	+62.24405	5.442	-20.57 ± 0.03	25.24	19.43 ± 0.64	F
131	JADES-GN-189.05777+62.23927	189.05777	+62.23927	5.443	-20.33 ± 0.05	25.60	7.50 ± 0.45	F
132	JADES-GN-189.08862+62.23949	189.08862	+62.23949	5.443	-19.83 ± 0.03	26.05	10.85 ± 0.45	F
133	JADES-GN-189.14305+62.21142	189.14305	+62.21142	5.446	-18.34 ± 0.08	26.37	4.37 ± 0.69	F
134	JADES-GN-189.18792+62.29720	189.18792	+62.29720	5.450	-19.18 ± 0.10	27.51	1.84 ± 0.27	F
135	JADES-GN-189.15552+62.20012	189.15552	+62.20012	5.456	-19.12 ± 0.03	25.94	4.15 ± 1.05	F
136	JADES-GN-189.15888+62.19685	189.15888	+62.19685	5.456	-19.17 ± 0.03	27.07	3.65 ± 0.39	F
137	JADES-GN-189.15551+62.20002	189.15551	+62.20002	5.457	-19.30 ± 0.06	26.07	8.81 ± 1.21	F
138	JADES-GN-189.06882+62.26887	189.06882	+62.26887	5.470	-19.87 ± 0.03	26.85	2.26 ± 0.33	F
139	JADES-GN-189.23458+62.19048	189.23458	+62.19048	5.484	-19.17 ± 0.03	27.86	3.43 ± 0.37	F
140	JADES-GN-189.14849+62.21166	189.14849	+62.21166	5.490	-18.89 ± 0.05	27.18	3.86 ± 0.58	F

Note. Coordinates are in ICRS (J2000.0). The typical uncertainty of grism spectroscopic redshifts (z_{spec}) is $\Delta z = 0.001$. The uncertainty of F444W magnitude is dominated by flux calibration and aperture correction, and we adopt a 5% noise floor. In the group ID column, "F" denotes field galaxies while other number IDs are assigned through our FoF clustering analysis (Section 5.2). HDF850.1 and five AGN candidates with broad Hα emission lines are not included in this table. The coordinates and redshifts of AGN candidates will be presented in a companion paper (E. Egami et al. 2023, in preparation).
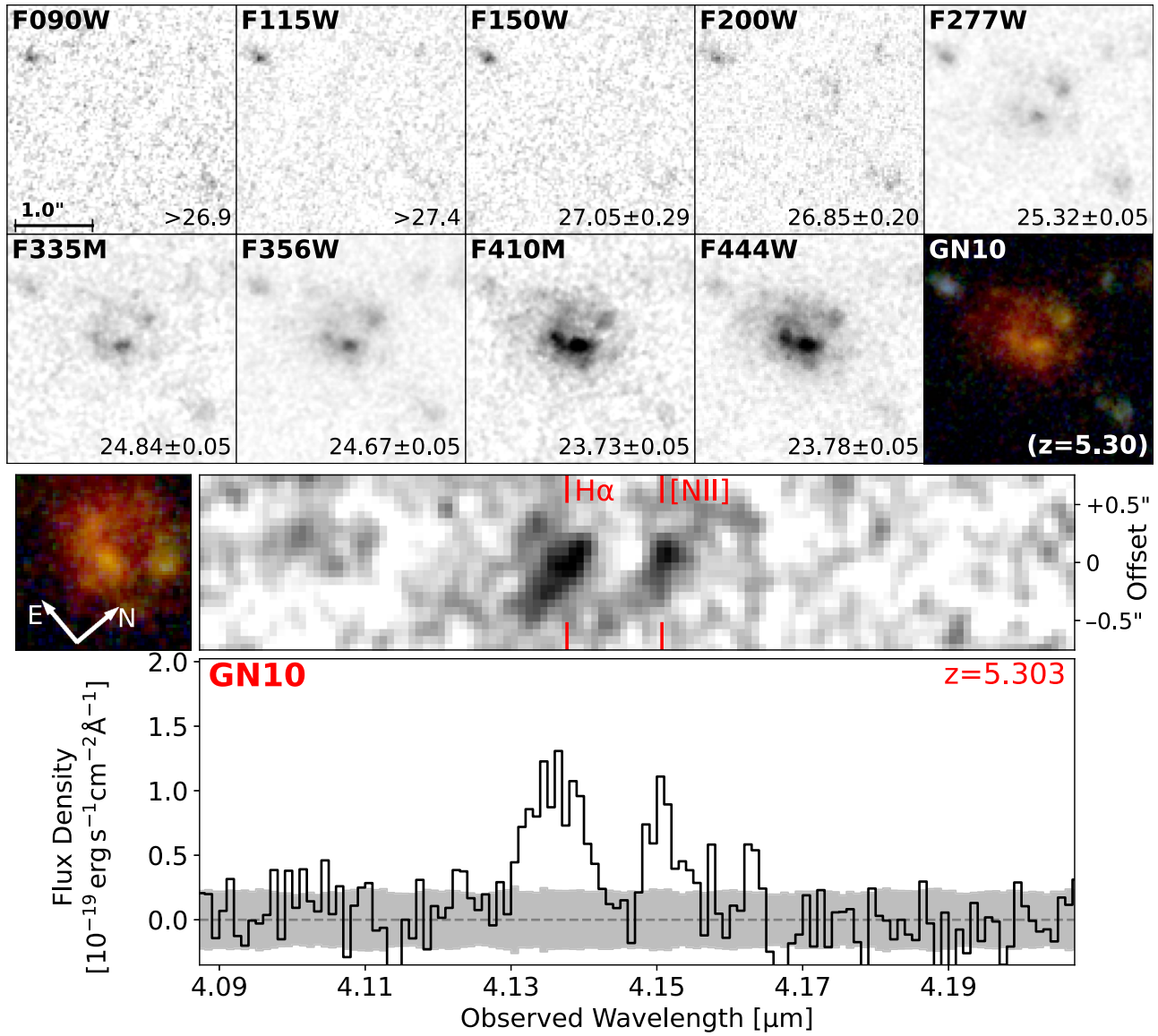
(This table is available in machine-readable form.)

Figure A2. Top: NIRCam images of GN10 in the F090W–F444W band. The brightness of GN10 in each band is noted in the lower right corner of each panel (unit: AB mag). Image sizes are $3'' \times 3''$ (north up, east left). The last panel shows the true-color NIRCam image. Bottom: NIRCam grism spectrum of GN10 (similar to those in Figures 6 and A1). Images are rotated to align with the dispersion direction. Hα and [N II] $\lambda6583$ line can be detected at $z = 5.303$, which are indicated by vertical red lines in 2D spectrum.
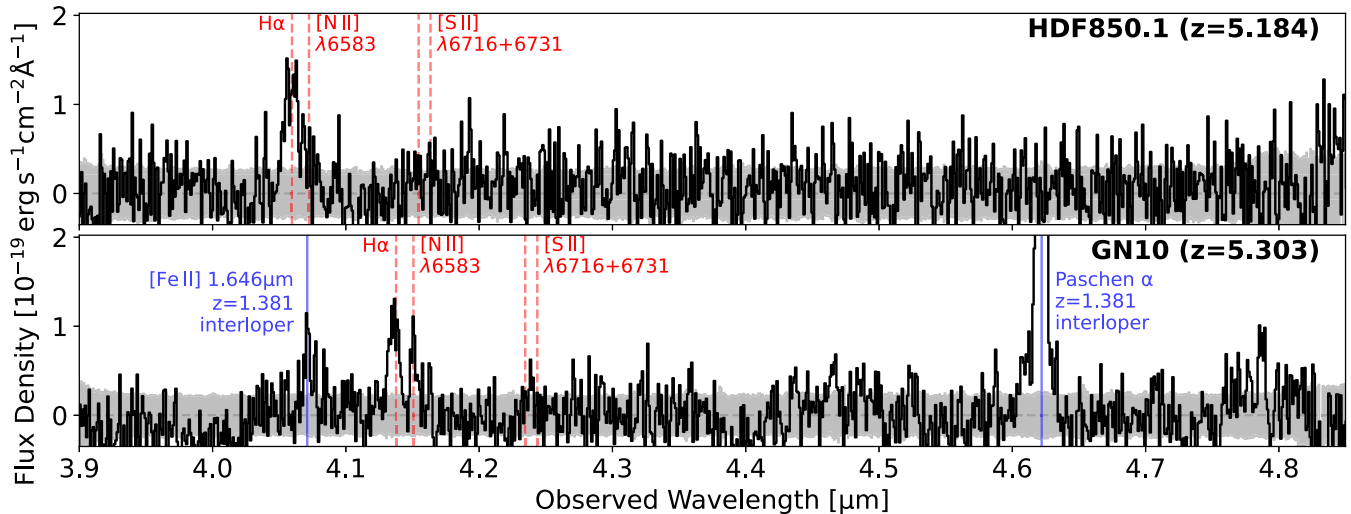

Figure A3. Full NIRCam 1D grism spectra of HDF850.1 (top) and GN10 (bottom). The expected wavelengths of Hα, [N II] $\lambda6583$, [S II] $\lambda6716$ and 6731 lines are labeled with dashed red lines. The full spectrum of GN10 is contaminated by a $z = 1.381$ galaxy (R.A.: 12:36:34.282, decl.: +62°14′00″.5; 10″ from GN10), whose [Fe II] $\lambda1.646$ μm and Paschen α lines are detected (indicated by the solid blue lines).

ORCID iDs

Fengwu Sun ⦿ https://orcid.org/0000-0002-4622-6617
Jakob M. Helton ⦿ https://orcid.org/0000-0003-4337-6211
Eiichi Egami ⦿ https://orcid.org/0000-0003-1344-9475
Kevin N. Hainline ⦿ https://orcid.org/0000-0003-4565-8239
George H. Rieke ⦿ https://orcid.org/0000-0003-2303-6519
Christopher N. A. Willmer ⦿ https://orcid.org/0000-0001-9262-9997
Daniel J. Eisenstein ⦿ https://orcid.org/0000-0002-2929-3121
Benjamin D. Johnson ⦿ https://orcid.org/0000-0002-9280-7594
Marcia J. Rieke ⦿ https://orcid.org/0000-0002-7893-6170
Brant Robertson ⦿ https://orcid.org/0000-0002-4271-0364
Sandro Tacchella ⦿ https://orcid.org/0000-0002-8224-4505
Stacey Alberts ⦿ https://orcid.org/0000-0002-8909-8782
William M. Baker ⦿ https://orcid.org/0000-0003-0215-1104
Rachana Bhatawdekar ⦿ https://orcid.org/0000-0003-0883-2226
Kristan Boyett ⦿ https://orcid.org/0000-0003-4109-304X
Andrew J. Bunker ⦿ https://orcid.org/0000-0002-8651-9879
Stephane Charlot ⦿ https://orcid.org/0000-0003-3458-2275
Zuyi Chen ⦿ https://orcid.org/0000-0002-2178-5471
Jacopo Chevallard ⦿ https://orcid.org/0000-0002-7636-0534
Emma Curtis-Lake ⦿ https://orcid.org/0000-0002-9551-0534
A. Lola Danhaive ⦿ https://orcid.org/0000-0002-9708-9958
Christa DeCoursey ⦿ https://orcid.org/0000-0002-4781-9078
Zhiyuan Ji ⦿ https://orcid.org/0000-0001-7673-2257
Jianwei Lyu ⦿ https://orcid.org/0000-0002-6221-1829
Roberto Maiolino ⦿ https://orcid.org/0000-0002-4985-3819
Wiphu Rujopakarn ⦿ https://orcid.org/0000-0002-0303-499X
Lester Sandles ⦿ https://orcid.org/0000-0001-9276-7062
Irene Shivaei ⦿ https://orcid.org/0000-0003-4702-7561
Hannah Übler ⦿ https://orcid.org/0000-0003-4891-0794
Chris Willott ⦿ https://orcid.org/0000-0002-4201-7367
Joris Witstok ⦿ https://orcid.org/0000-0002-7595-121X

References

Akins, H. B., Fujimoto, S., Finlator, K., et al. 2022, ApJ, 934, 64
Alcalde Pampliega, B., Pérez-González, P. G., Barro, G., et al. 2019, ApJ, 876, 135
Armus, L., Charmandaris, V., & Soifer, B. T. 2020, NatAs, 4, 467
Arrabal Haro, P., Rodríguez Espinosa, J. M., Muñoz-Tuñón, C., et al. 2018, MNRAS, 478, 3740
Astropy Collaboration, Price-Whelan, A. M., Sipőcz, B. M., et al. 2018, AJ, 156, 123
Astropy Collaboration, Robitaille, T. P., Tollerud, E. J., et al. 2013, A&A, 558, A33
Barger, A. J., Cowie, L. L., Brandt, W. N., et al. 2002, AJ, 124, 1839
Barger, A. J., Cowie, L. L., & Wang, W. H. 2008, ApJ, 689, 687
Barrufet, L., Oesch, P. A., Weibel, A., et al. 2023, MNRAS, 522, 449
Behroozi, P., Wechsler, R. H., Hearin, A. P., & Conroy, C. 2019, MNRAS, 488, 3143
Berta, S., Magnelli, B., Nordon, R., et al. 2011, A&A, 532, A49
Béthermin, M., Fudamoto, Y., Ginolfi, M., et al. 2020, A&A, 643, A2
Bond, J. R., Kofman, L., & Pogosyan, D. 1996, Natur, 380, 603
Boquien, M., Burgarella, D., Roehlly, Y., et al. 2019, A&A, 622, A103
Bradley, L., Sipőcz, B., Robitaille, T., et al. 2022, astropy/photutils: v1.5.0, Zenodo, doi:10.5281/zenodo.6825092
Brammer, G. B., van Dokkum, P. G., & Coppi, P. 2008, ApJ, 686, 1503
Bruzual, G., & Charlot, S. 2003, MNRAS, 344, 1000
Bunker, A. J., Saxena, A., Cameron, A. J., et al. 2023, A&A, 677, 88
Calvi, R., Castignani, G., & Dannerbauer, H. 2023, A&A, 678, 15
Calvi, R., Dannerbauer, H., Arrabal Haro, P., et al. 2021, MNRAS, 502, 4558
Calzetti, D., Armus, L., Bohlin, R. C., et al. 2000, ApJ, 533, 682
Cameron, A. J., Saxena, A., Bunker, A. J., et al. 2023, A&A, 677, 115
Carnall, A. C., McLure, R. J., Dunlop, J. S., & Davé, R. 2018, MNRAS, 480, 4379
Carnall, A. C., McLure, R. J., Dunlop, J. S., et al. 2023, Natur, 619, 716
Casey, C. M. 2016, ApJ, 824, 36
Casey, C. M., Scoville, N. Z., Sanders, D. B., et al. 2014, ApJ, 796, 95
Casey, C. M., Zavala, J. A., Manning, S. M., et al. 2021, ApJ, 923, 215
Castignani, G., Chiaberge, M., Celotti, A., Norman, C., & De Zotti, G. 2014, ApJ, 792, 114
Castignani, G., Combes, F., Salomé, P., et al. 2019, A&A, 623, A48
Chabrier, G. 2003, PASP, 115, 763
Chapin, E. L., Pope, A., Scott, D., et al. 2009, MNRAS, 398, 1793
Chen, C.-C., Gao, Z.-K., Hsu, Q.-N., et al. 2022, ApJL, 939, L7
Chen, C.-C., Smail, I., Swinbank, A. M., et al. 2015, ApJ, 799, 194
Chen, Z., Stark, D. P., Endsley, R., et al. 2023, MNRAS, 518, 5607
Cheng, C., Huang, J.-S., Smail, I., et al. 2023, ApJL, 942, L19
Cheng, C., Yan, H., Huang, J.-S., et al. 2022, ApJL, 936, L19
Chiang, Y.-K., Overzier, R., & Gebhardt, K. 2013, ApJ, 779, 127
Chiang, Y.-K., Overzier, R. A., Gebhardt, K., & Henriques, B. 2017, ApJL, 844, L23
Cicone, C., Maiolino, R., Gallerani, S., et al. 2015, A&A, 574, A14
Combes, F., Rex, M., Rawle, T. D., et al. 2012, A&A, 538, L4
Cowie, L. L., Barger, A. J., Hsu, L. Y., et al. 2017, ApJ, 837, 139
Cowie, L. L., Barger, A. J., Wang, W. H., & Williams, J. P. 2009, ApJL, 697, L122
da Cunha, E., Charlot, S., & Elbaz, D. 2008, MNRAS, 388, 1595
Daddi, E., Bournaud, F., Walter, F., et al. 2010, ApJ, 713, 686
De Rossi, M. E., Rieke, G. H., Shivaei, I., Bromm, V., & Lyu, J. 2018, ApJ, 869, 4
Dole, H., Lagache, G., & Puget, J. L. 2003, ApJ, 585, 617
Dole, H., Rieke, G. H., Lagache, G., et al. 2004, ApJS, 154, 93
Downes, D., Neri, R., Greve, A., et al. 1999, A&A, 347, 809
Draine, B. T., & Li, A. 2007, ApJ, 657, 810
Dudzevičiūtė, U., Smail, I., Swinbank, A. M., et al. 2020, MNRAS, 494, 3828
Duncan, K. J., Windhorst, R. A., Koekemoer, A. M., et al. 2023, MNRAS, 522, 4548
Dunlop, J. S., McLure, R. J., Yamada, T., et al. 2004, MNRAS, 350, 769
Eisenstein, D. J., Willott, C., Alberts, S., et al. 2023, arXiv:2306.02465
Fernández-Soto, A., Lanzetta, K. M., & Yahil, A. 1999, ApJ, 513, 34
Franco, M., Elbaz, D., Béthermin, M., et al. 2018, A&A, 620, A152
Fudamoto, Y., Oesch, P. A., Faisst, A., et al. 2020, A&A, 643, A4
Fujimoto, S., Kohno, K., Ouchi, M., et al. 2023, arXiv:2303.01658
Fujimoto, S., Ouchi, M., Ferrara, A., et al. 2019, ApJ, 887, 107
Fujimoto, S., Ouchi, M., Shibuya, T., & Nagai, H. 2017, ApJ, 850, 83
Fujimoto, S., Silverman, J. D., Bethermin, M., et al. 2020, ApJ, 900, 1
Gaia Collaboration, Brown, A. G. A., Vallenari, A., et al. 2021, A&A, 649, A1
Giménez-Arteaga, C., Oesch, P. A., Brammer, G. B., et al. 2023, ApJ, 948, 126
Ginolfi, M., Jones, G. C., Béthermin, M., et al. 2020, A&A, 633, A90
Gómez-Guijarro, C., Elbaz, D., Xiao, M., et al. 2022a, A&A, 658, A43
Gómez-Guijarro, C., Elbaz, D., Xiao, M., et al. 2022b, A&A, 659, A196
Gómez-Guijarro, C., Toft, S., Karim, A., et al. 2018, ApJ, 856, 121
Grogin, N. A., Kocevski, D. D., Faber, S. M., et al. 2011, ApJS, 197, 35
Gullberg, B., Smail, I., Swinbank, A. M., et al. 2019, MNRAS, 490, 4956
Haider, M., Steinhauser, D., Vogelsberger, M., et al. 2016, MNRAS, 457, 3024
Hainline, K. N., Johnson, B. D., Robertson, B., et al. 2023, arXiv:2306.02468
Helton, J. M., Sun, F., Woodrum, C., et al. 2023, arXiv:2302.10217
Herard-Demanche, T., Bouwens, R. J., Oesch, P. A., et al. 2023, arXiv:2309.04525
Herrera-Camus, R., Förster Schreiber, N., Genzel, R., et al. 2021, A&A, 649, A31
Hodge, J. A., & da Cunha, E. 2020, RSOS, 7, 200556
Hogg, D. W., Blandford, R., Kundic, T., Fassnacht, C. D., & Malhotra, S. 1996, ApJL, 467, L73
Horne, K. 1986, PASP, 98, 609
Hughes, D. H., Serjeant, S., Dunlop, J., et al. 1998, Natur, 394, 241
Illingworth, G. 2015, Hubble Legacy Fields ("HLF"), STScI/MAST, doi:10.17909/T91019
Ivison, R. J., Smail, I., Le Borgne, J. F., et al. 1998, MNRAS, 298, 583
Jin, S., Sillassen, N. B., Magdis, G. E., et al. 2023, A&A, 670, L11
Jullo, E., Kneib, J. P., Limousin, M., et al. 2007, NJPh, 9, 447
Kaiser, N. 1987, MNRAS, 227, 1
Kashino, D., Lilly, S. J., Matthee, J., et al. 2023, ApJ, 950, 66
Kennicutt, R. C., & Evans, N. J. 2012, ARA&A, 50, 531
Koekemoer, A. M., Faber, S. M., Ferguson, H. C., et al. 2011, ApJS, 197, 36
Kokorev, V., Jin, S., Magdis, G. E., et al. 2023, ApJL, 945, L25
Kokorev, V. I., Magdis, G. E., Davidzon, I., et al. 2021, ApJ, 921, 40
Lambert, T. S., Posses, A., Aravena, M., et al. 2023, MNRAS, 518, 3183
Lang, P., Schinnerer, E., Smail, I., et al. 2019, ApJ, 879, 54
Le Bail, A., Daddi, E., Elbaz, D., et al. 2023, arXiv:2307.07599
Le Fèvre, O., Béthermin, M., Faisst, A., et al. 2020, A&A, 643, A1

Maiolino, R., Carniani, S., Fontana, A., et al. 2015, MNRAS, 452, 54
Matthee, J., Naidu, R. P., Brammer, G., et al. 2023, arXiv:2306.05448
McKinney, J., Manning, S. M., Cooper, O. R., et al. 2023, ApJ, 956, 72
Meurer, G. R., Heckman, T. M., & Calzetti, D. 1999, ApJ, 521, 64
Miller, T. B., Whitaker, K. E., Nelson, E. J., et al. 2022, ApJL, 941, L37
Mosleh, M., Tacchella, S., Renzini, A., et al. 2017, ApJ, 837, 2
Narayanan, D., Davé, R., Johnson, B. D., et al. 2018, MNRAS, 474, 1718
Narayanan, D., Turk, M., Feldmann, R., et al. 2015, Natur, 525, 496
Navarro, J. F., Frenk, C. S., & White, S. D. M. 1996, ApJ, 462, 563
Nelson, E. J., Suess, K. A., Bezanson, R., et al. 2023, ApJL, 948, L18
Nelson, E. J., van Dokkum, P. G., Momcheva, I. G., et al. 2016, ApJL, 817, L9
Neri, R., Downes, D., Cox, P., & Walter, F. 2014, A&A, 562, A35
Nguyen, H. T., Schulz, B., Levenson, L., et al. 2010, A&A, 518, L5
Noll, S., Burgarella, D., Giovannoli, E., et al. 2009, A&A, 507, 1793
Oesch, P. A., Bouwens, R. J., Carollo, C. M., et al. 2010, ApJL, 709, L21
Oesch, P. A., Brammer, G., Naidu, R. P., et al. 2023, MNRAS, 525, 2864
Oteo, I., Cepa, J., Bongiovanni, Á., et al. 2013, A&A, 554, L3
Peng, C. Y., Ho, L. C., Impey, C. D., & Rix, H.-W. 2010, AJ, 139, 2097
Penner, K., Dickinson, M., Pope, A., et al. 2012, ApJ, 759, 28
Pérez-González, P. G., Barro, G., Annunziatella, M., et al. 2023, ApJL, 946, L16
Pérez-González, P. G., Cava, A., Barro, G., et al. 2013, ApJ, 762, 46
Pizzati, E., Ferrara, A., Pallottini, A., et al. 2020, MNRAS, 495, 160
Pizzati, E., Ferrara, A., Pallottini, A., et al. 2023, MNRAS, 519, 4608
Pope, A., Borys, C., Scott, D., et al. 2005, MNRAS, 358, 149
Popesso, P., Concas, A., Cresci, G., et al. 2023, MNRAS, 519, 1526
Popping, G., Puglisi, A., & Norman, C. A. 2017, MNRAS, 472, 2315
Rawle, T. D., Egami, E., Bussmann, R. S., et al. 2014, ApJ, 783, 59
Reddy, N. A., Oesch, P. A., Bouwens, R. J., et al. 2018, ApJ, 853, 56
Riechers, D. A., Hodge, J. A., Pavesi, R., et al. 2020, ApJ, 895, 81
Rieke, G. H., Alonso-Herrero, A., Weiner, B. J., et al. 2009, ApJ, 692, 556
Rieke, M., Robertson, B., Tacchella, S., et al. 2023a, ApJS, 269, 16
Rieke, M. J., Kelly, D. M., Misselt, K., et al. 2023b, PASP, 135, 028001
Rigby, J., Perrin, M., McElwain, M., et al. 2023, PASP, 135, 048001
Rodighiero, G., Bisigello, L., Iani, E., et al. 2023, MNRAS, 518, L19
Rowan-Robinson, M. 2003, MNRAS, 345, 819
Rujopakarn, W., Daddi, E., Rieke, G. H., et al. 2019, ApJ, 882, 107
Rujopakarn, W., Williams, C. C., Daddi, E., et al. 2023, ApJL, 948, L8
Sanders, D. B., Soifer, B. T., Elias, J. H., et al. 1988, ApJ, 325, 74
Sanders, R. L., Shapley, A. E., Topping, M. W., Reddy, N. A., & Brammer, G. B. 2023, ApJ, 955, 54
Schreiber, C., Elbaz, D., Pannella, M., et al. 2018, A&A, 609, A30
Schreiber, C., Pannella, M., Elbaz, D., et al. 2015, A&A, 575, A74
Serjeant, S., & Marchetti, L. 2014, MNRAS, 443, 3118
Shapley, A. E., Reddy, N. A., Sanders, R. L., Topping, M. W., & Brammer, G. B. 2023, ApJL, 950, L1
Shibuya, T., Ouchi, M., & Harikane, Y. 2015, ApJS, 219, 15
Simpson, J. M., Swinbank, A. M., Smail, I., et al. 2014, ApJ, 788, 125
Smail, I., Dudzeviciute, U., Gurwell, M., et al. 2023, ApJ, 958, 36
Smail, I., Dudzevičiūtė, U., Stach, S. M., et al. 2021, MNRAS, 502, 3426
Smail, I., Ivison, R. J., & Blain, A. W. 1997, ApJL, 490, L5
Speagle, J. S., Steinhardt, C. L., Capak, P. L., & Silverman, J. D. 2014, ApJS, 214, 15
Staguhn, J. G., Kovács, A., Arendt, R. G., et al. 2014, ApJ, 790, 77
Stefanon, M., Labbé, I., Oesch, P. A., et al. 2021, ApJS, 257, 68
Steinhardt, C. L., Kokorev, V., Rusakov, V., Garcia, E., & Sneppen, A. 2023, ApJ, 951, 40
Struble, M. F., & Rood, H. J. 1999, ApJS, 125, 35
Suess, K. A., Bezanson, R., Nelson, E. J., et al. 2022, ApJL, 937, L33
Suess, K. A., Kriek, M., Price, S. H., & Barro, G. 2019, ApJ, 877, 103
Sun, F., Egami, E., Fujimoto, S., et al. 2022a, ApJ, 932, 77
Sun, F., Egami, E., Pérez-González, P. G., et al. 2021a, ApJ, 922, 114
Sun, F., Egami, E., Pirzkal, N., et al. 2022b, ApJL, 936, L8
Sun, F., Egami, E., Pirzkal, N., et al. 2023, ApJ, 953, 53
Sun, F., Egami, E., Rawle, T. D., et al. 2021b, ApJ, 908, 192
Tacchella, S., Carollo, C. M., Förster Schreiber, N. M., et al. 2018, ApJ, 859, 56
Tacchella, S., Eisenstein, D. J., Hainline, K., et al. 2023, ApJ, 952, 74
Trenti, M., & Stiavelli, M. 2008, ApJ, 676, 767
Walter, F., Decarli, R., Carilli, C., et al. 2012, Natur, 486, 233
Wang, F., Yang, J., Hennawi, J. F., et al. 2023, ApJL, 951, L4
Wang, T., Schreiber, C., Elbaz, D., et al. 2019, Natur, 572, 211
Wang, W. H., Cowie, L. L., & Barger, A. J. 2004, ApJ, 613, 655
Weaver, J. R., Davidzon, I., Toft, S., et al. 2023, A&A, 677, 184
Whitaker, K. E., Ashas, M., Illingworth, G., et al. 2019, ApJS, 244, 16
Williams, C. C., Labbe, I., Spilker, J., et al. 2019, ApJ, 884, 154
Woodrum, C., Rieke, M., Ji, Z., et al. 2023, arXiv:2310.18464
Wu, Y., Cai, Z., Sun, F., et al. 2023, ApJL, 942, L1
Yamaguchi, Y., Kohno, K., Hatsukade, B., et al. 2019, ApJ, 878, 73
Zavala, J. A., Casey, C. M., Spilker, J., et al. 2022, ApJ, 933, 242